Particuology 82 (2023) 25–47

Contents lists available at ScienceDirect

Particuology

journal homepage: www.elsevier.com/locate/partic

Predictions of the P1 approximation for radiative heat transfer in heterogeneous granular media

Jelena Mačak [a, b, *], Christoph Goniva [a], Stefan Radl [b]

[a] DCS Computing GmbH, 4020, Linz, Austria
[b] Graz University of Technology, Institute of Process and Particle Engineering, 8010, Graz, Austria

ARTICLE INFO

Article history:
Received 8 November 2022
Received in revised form
20 December 2022
Accepted 4 January 2023
Available online 31 January 2023

Keywords:
CFD-DEM
Thermal radiation
Coarse-graining
P1
Pebble bed nuclear reactor

ABSTRACT

The P1 approximation is a computationally efficient model for thermal radiation. Here, we present a P1 formulation in the context of the combined computational fluid dynamics and discrete element method (CFD-DEM), including closures for dependent scattering and coarse-graining. Using available analytical and semi-analytical solutions, we find agreement for steady-state and transient quantities in size-disperse systems. Heat flux is identified as the most sensitive quantity to predict, displaying unphysical spatial oscillations. These oscillations are due to a temperature slip at the locations of abrupt change in solid fraction. We propose two techniques that mitigate this effect: smoothing of the radiative properties, and pseudo-scattering. Furthermore, using up to a million times enlarged particles, we demonstrate practically limitless compatibility with coarse-graining. Finally, we compare predictions made with our code to experimental data for a pebble bed under vacuum conditions, and in presence of nitrogen. We find that a carefully calibrated simulation can replicate trends observed in experiments, with relative temperature error of less than 10%.

1. Introduction

1.1. Motivation

Under the impending climate crisis, many high-temperature processes need to be revised or replaced to maximize energy efficiency and minimize CO2 emissions. Granular media happen to be a part of many currently explored concepts to achieve this vision.

For example, a pebble bed is regarded as one of the most promising very-high temperature nuclear reactor designs (Stöcker & Niessen, 1997). Natural and ceramic particles are proposed as a low-cost heat transfer media in concentrating solar plants (Siegel et al., 2014). Solar energy is also studied as a means to drive chemical reactions, e.g. in particle suspensions (Kopping et al., 2019) or in rotary kilns (Moumin et al., 2019). Further examples include processes such as pyrolysis and gasification of biomass (Peters et al., 2019; Zhong et al., 2016).

All aforementioned applications are affected by thermal radiation. The solution of accurate radiation models tends to be computationally expensive, which is unfortunately incompatible with typical requirements of industrial or applied research. Also, the scarcity of relevant verification and validation cases does not allow the use of various approximate models with sufficient confidence. This leads to the fact that radiative energy transfer is often grossly mis-predicted, or even completely neglected.

The main purpose of our present study is to carefully evaluate the predictive capabilities of the P1 approximation (Jeans, 1917; Modest, 2013) for gas-particle systems. Due to its simplicity, the P1 model is extremely computationally efficient, and also compatible with techniques such as coarse-graining and multi-threading. Recent Monte Carlo ray tracing studies of packed beds (Liu et al., 2021) confirm that the radiative transfer in random assemblies of particles is diffusive, suggesting a solid physical basis for applying the P1 model in a wide range of industrial settings.

1.2. State-of-the-art radiation models

Literature on radiation, and radiation in granular media is vast and cannot be covered here completely. A detailed overview can be found in books on radiative heat transfer (Howell et al., 2010; Modest, 2013). In what follows, we briefly review the most

* Corresponding author. DCS Computing GmbH, 4020, Linz, Austria.
E-mail address: jelena.macak@dcs-computing.com (J. Mačak).

https://doi.org/10.1016/j.partic.2023.01.003

important concepts that are needed to correctly perceive our current contribution.

Numerical models for radiative heat transfer in granular media can be roughly grouped into discrete and continuum-based models. Discrete models handle particles as individual objects which engage in radiative heat exchange via their surfaces. Continuum-based models treat the mixture of particles and the ambient gas as one continuous medium with effective attenuation properties distributed between the phases.

1.2.1. Discrete models

Discrete models are based on evaluation of view factors between individual particles. A view factor is a geometrical quantity which represents the amount of energy which, after being emitted by one particle, arrives at the surface of another particle.

The accuracy-standard for view factor calculations is the Monte Carlo ray tracing (MCRT), described, for example, in (Amberger et al., 2013). While being accurate, MCRT is extremely computationally demanding and therefore justified only for cases where the radiative heat transfer is the sole focus. Recent examples include assessment of view factor correlations to solid fraction in a double-screw reactor (Qi & Wright, 2018), and investigation of polydispersity in a free-falling particle solar receiver (Chen et al., 2022).

View factors can also be calculated using the projection method (Forgber & Radl, 2018), or, as of recent, the machine learning-based concepts (Tausendschöen et al., 2023; Tausendschöen & Radl, 2021). While the projection method is limited to systems with relatively small numbers of particles, machine learning significantly improves computational speeds for mono-, bi- and polydisperse static systems. However, the accuracy is dependent on the quality of the training data, and the method is yet not available for coarse-graining and multi-threading.

Industry demands for efficiency created approximate models, such as (Peters, 2002; Peters et al., 2019), where the view factor is taken as the ratio of surface areas of neighbouring particles. Even simpler, the model proposed in (Zhou et al., 2009) abandons the view factors altogether and estimates the radiative contribution to a particle using the average local temperature. Recently, such a model was used for a coarse-grained reacting flow (Wang & Shen, 2022), and for biomass gasification in a bubbling fluidized bed (Kong et al., 2022). Both studies validated the heat transfer model with experimental data in the range of 20 °C–90 °C, even though the operating temperature of the considered fluidized beds exceeds 1000 K. Since the radiation contribution becomes significant at above 500 K, validation at lower temperatures might lead to inaccurate conclusions.

1.2.2. Continuum-based models

Continuum-based models are derived from the radiative transfer equation (RTE). While, according to the definition, RTE is limited only to homogeneous media, it has been frequently applied to gas-particle systems (Viskanta & Mengüç, 1987). Even more so, the extension of RTE to heterogeneous media (Gusarov, 2009) is recommended only for cases with partially transparent particles. Recently, the validity of the RTE for spatially random assemblies of particles was also confirmed by Monte Carlo ray tracing simulations (Liu et al., 2021).

In its general form, the RTE is a function of 3 spatial coordinates, 2 angular coordinates (i.e., the zenith and azimuthal angle), and wavelength. The angular dependency is treated either by the discrete ordinates method (DOM) or by the spherical harmonics approximation.

The discrete ordinates method (Chandrasekhar, 1950; Modest, 2013) features additional discretization of the domain along a set of spatial angles. The DOM is commonly applied to model soot particles and combustion gases (Viskanta & Mengüç, 1987). Other examples include water droplets in fire-suppression systems (Oluwole et al., 2021), wet biomass carbonization in a rotary kiln (Tavakkol et al., 2021), and solar gasification of coal-coke in a circulating fluidized bed (Bellan et al., 2018).

Alternatively, in the family of Pn-approximations, the RTE is developed using spherical harmonics of the n-th order. Simplest, and most popular, is the first-order approximation: the P1 (Jeans, 1917; Modest, 2013). Here, the multi-dimensional RTE is reduced to a single diffusion-like scalar equation for radiative intensity, yielding a significant efficiency improvement compared to the DOM. However, since the angular dependency is completely lost, P1 is accurate only for an isotropic radiative field (Dombrovsky, 1997; Dombrovsky, 2010; Modest, 2013; Viskanta & Mengüç, 1987).

Yet, good agreement with experiments is reported for various gas-particle systems. For example, both P1 and DOM were used to model monodisperse and polydisperse mixtures of fuel particles for underwater combustion. Tested against experiments, DOM performed only slightly better than P1. Furthermore, P1 was applied to model biomass gasification in an Euler-Euler simulation (Liu et al., 2013), in an Euler-Lagrange simulation (Ku et al., 2015), and recently even in an Euler-Lagrange simulation with coarse-graining (Yang et al., 2022), all agreeing with experimental data. However, since the aforementioned studies focused on chemical reactions, critical details regarding the radiation modeling (i.e., treatment of the dependent scattering, closure for coarse-graining) were omitted.

On the other hand, P1 is also reported to be in disagreement with experiments. Inaccurate heating rates where found in an attempt to simulate transient heat-up of a directly irradiated bubbling fluidized bed (Díaz-Heras et al., 2021). While a steady rise in temperature was observed in the experiment, the simulation settled earlier at a lower temperature. A reason for this deviation might be the approximate boundary condition for an imposed radiative heat flux used in (Díaz-Heras et al., 2021).

1.3. Goals

The purpose of this study is twofold: 1) to verify the current implementation of the P1 model in the context of a coarse-grained CFD-DEM approach, and 2) to test the applicability of the P1 model to general gas-particle systems with size-disperse particles.

For verification, we consider (i) the steady-state temperature profile, (ii) the steady-state heat flux, and also (iii) the transient heat-up process of a gas-particle mixture.

As a benchmark for the steady-state, we use the well-known exact solution for a homogeneous gray medium between two infinite black plates (Heaslet & Warming, 1965). We compare the results obtained for a) a uniform monodisperse bed, b) a uniform bidisperse bed, and c) a randomly packed polydisperse bed.

To verify the transient temperature profile, we study: a) a solitary particle in an isothermal black enclosure, and b) a packed bed placed between two isothermal black plates. For the former, we find an analytical solution alongside important dimensionless parameters, and for the latter, we use a semi-analytical solution for a continuous gray medium (Lipiński & Steinfeld, 2005).

Our second goal is to determine whether the P1 model is appropriate for describing radiative heat transfer in granular flows. Being an approximation of the 1st order, P1 model compromises precision. Based on comparisons with other methods, excellent agreement is possible for optically thick media, and for an isotropic radiative field (Viskanta & Mengüç, 1987). Both of the requirements are tested in our present study: first, we estimate the number of particles needed for reaching the opacity limit, and second, to challenge the isotropy condition, we derive an approximate

solution for the radiative balance at the interface between two media of disparate optical thickness. This allows us to quantify the influence of variations in void fraction when making predictions with the P1 model.

Finally, we also show how the P1 model compares with experimental data: (i) in a packed pebble bed under vacuum (De Beer, 2014), and (ii) in a packed pebble bed cooled with nitrogen (Stöcker & Niessen, 1997).

Our present study is limited to gray particles, isotropic scattering, and transparent gases. Furthermore, due to compatibility with available verification and validation test cases, only densely packed systems were considered. While the main findings of the study will also hold true for moving granular systems with moderate variations in void fraction, future research is still needed to further probe the reliability of the P1 model: this might be especially important for flows involving extreme gradients in the void fraction field. Note that the temporal fluctuations will not affect the radiative energy transfer, since there are no time derivatives in the P1 model.

1.4. Content

The manuscript is organized as follows:

- The mathematical model is detailed in section 2. To start, we define the radiative properties of the involved phases (including closures for dependent scattering and coarse-graining) in subsection 2.1. Next, we formulate the P1 model in subsection 2.2. The present formulation gives rise to unphysical heat flux oscillations at locations of change in void fraction. Numerical strategies employed to control these oscillations are given in subsection 2.3.
- Results are collected in section 3. Assessment of the opacity of granular media is presented first, in subsection 3.1, as it contains definitions necessary for understanding the rest of the text. Next, verification with the steady-state analytical solution is given in subsection 3.2. This steady-state solution is further expanded in order to study the effects of non-uniform void fraction in subsection 3.3. In addition to thermal radiation, validation cases presented in subsection 3.4 feature other modes of heat transfer: i.e., conduction in subsection 3.4.1, and conduction and free convection in subsection 3.4.2.
- Major findings are summarized in section 4.
- Verification of the transient heat up process is given separately in Appendix A, followed by a brief comment on the influence of the particle size and absorption properties in Appendix B. Furthermore, verification of the boundary conditions for imposed radiative heat flux, and isothermal gray walls are carried out respectively in Appendix C, and Appendix D.

2. Mathematical model

The mathematical model presented in this chapter deals exclusively with thermal radiation. Radiative properties of a gas-particle mixture are described in subsection 2.1. Formulation of the P1 model follows in subsection 2.2. Numerical strategies employed to control the unphysical heat flux oscillations are given in subsection 2.3.

The model is implemented in the software CFDEMCoupling (CFDEMcoupling open source CFD, 2011; Goniva et al., 2012). For particle calculations we use LIGGGHTS (Kloss et al., 2012; LIGGGHTS open source DEM particle, 2011), and as the basis for the fluid flow solution we use OpenFOAM (Weller et al., 1998; Greenshields, 2018; OpenFOAM v6 C++ Source Guide, 2018). A more detailed description of the CFD-DEM procedure and the associated governing equations can be found in a previous work of ours (Mačak et al., 2021), or in a large number of other references (Goniva et al., 2012; Norouzi et al., 2016; Zhou et al., 2010).

2.1. Radiative properties

Radiative properties (Table 1) indicate how much of the radiative energy is emitted, absorbed, or scattered by a medium. Media present in a typical industrial scenario includes particles, interstitial gas, and surfaces of the enclosure walls.

Generally, radiative properties change with wavelength, solid angle, and temperature. We circumvent these dependencies by employing the widely-employed gray body assumption.

Under local thermodynamic equilibrium, emission and absorption properties are interchangeable (Howell et al., 2010). This is commonly exploited to reduce the number of variables. According to the standard practice, particles and gases are described with their absorption properties, while emissivity (ε in Table 1) is used for the wall boundaries. Additionally, walls are considered gray and opaque, allowing the wall reflectivity to be replaced by a relation of the emissivity: $\varrho_w = 1 - \varepsilon_w$.

The following two sections provide a more detailed description of the radiative properties of the involved phases.

2.1.1. Particle properties

Radiative properties of a single particle are measured in terms of extinction efficiency Q_{ext}, scattering efficiency Q_{sca}, and scattering phase function Φ_s (Howell et al., 2010; Modest, 2013).

The extinction efficiency represents the total attenuation of a radiative beam by a particle, due to both scattering and absorption:

$$Q_{ext} = Q_{sca} + Q_{abs}. \tag{1}$$

The scattering efficiency, Q_{sca}, expresses the amount of radiative energy that is scattered away by a particle, while the scattering phase function, $\Phi_s(\Theta)$, specifies how the scattered energy is distributed across the spatial angle Θ. In the P1 approximation, the scattering phase function reduces to the following angle-independent relation:

$$\Phi_s \equiv 3 - A_1. \tag{2}$$

The asymmetry factor, A_1, stems from the cosine of the average scattering angle (Howell et al., 2010; Modest, 2013), and can acquire values in the range of -1 to 1. Negative values correspond to backward scattering, positive values to forward scattering, and $A_1 = 0$ to isotropic scattering.

The absorption efficiency Q_{abs} – which represents the relative amount of energy that is absorbed or emitted by a particle – cannot be directly measured. Instead, it is evaluated from Eq. (1).

Most industrial applications feature particles that are large compared to the incoming radiation wavelength. For large particles, the following relations hold true:

$$\begin{aligned} Q_{ext} &= 1, \\ Q_{sca} &= \varrho_p, \end{aligned} \tag{3}$$

i.e., the extinction efficiency always equals 1, and the scattering efficiency equals the reflectivity of the material (Howell et al., 2010; Modest, 2013). Moreover, following from Eqs. (1) and (3), the absorption efficiency will equal the particle material's emissivity:

$$Q_{abs} = 1 - \varrho_p = \varepsilon_p. \tag{4}$$

Table 1
Overview of radiative properties of the involved phases.

Function	Solid surface	Particle	Gas	Gas-particle mixture
scattering	reflectivity ϱ [−]	scattering efficiency Q_{sca} [−], scattering phase function Φ_s [−]	scattering coefficient σ_f [1 /m]	effective scattering coefficient σ_{eff} [1 /m]
absorption	absorptivity α [−]	absorption efficiency Q_{abs} [−]	absorption coefficient κ_f [1 /m]	absorption coefficient κ [1 /m]
emission*	emissivity ε ($=\alpha$) [−]	absorption efficiency Q_{abs} [−]	absorption coefficient κ_f [1 /m]	–

*assuming local thermodynamic equilibrium.

2.1.2. Continuum properties

Radiative properties of continua (i.e., media assumed to have continuous properties, such as gases or liquids) are defined per unit length. Within a fluid, emission and absorption are described with the absorption coefficient κ_f, and scattering is described with the scattering coefficient σ_f. While some gases, such as combustion products, significantly contribute to absorption and emission, scattering from a gas is generally considered negligible (Howell et al., 2010; Modest, 2013; Viskanta & Mengüç, 1987). However, for numerical reasons described in subsection 2.3, we also include a scattering coefficient for the gaseous phase. For air, this amounts to $\sigma_f = 1.23 \times 10^{-5}\ \mathrm{m}^{-1}$ (Penndorf, 1957).

Continuum-based radiation models (based on solving the radiative transfer equation) view the mixture of gas and particles as a continuum. The collective absorption coefficient is found by summing up the fluid and particle contributions:

$$\kappa = \kappa_f + \kappa_p. \tag{5}$$

In the expression for the effective scattering coefficient:

$$\sigma_{eff} = 3\sigma_f + \sigma_p(3 - A_1), \tag{6}$$

the particle contribution is additionally corrected for anisotropy with Eq. (2). Emission is accounted for separately for each phase (see subsection 2.2).

Eqs. (5) and (6) call for particle properties specified as attenuation coefficients. For a collection of N_p particles, enclosed within a volume V, the attenuation coefficients follow from:

$$\langle \beta_p, \sigma_p, \kappa_p \rangle = \frac{1}{(1-\varphi_p)V} \sum_{i=1}^{N_p} \langle Q_{ext,i}, Q_{sca,i}, Q_{abs,i} \rangle \frac{d_{p,i}^2 \pi}{4}, \tag{7}$$

where β_p, σ_p, and κ_p are the particle extinction, scattering, and absorption coefficient, each calculated using the respective efficiency. Here, subscript i denotes the individual particles.

The equation above holds true for the volume of the entire enclosure. In our simulations, we apply it to the volume of a single computational cell to account for the spatial heterogeneity of a typical gas-particle system. For this purpose, particle properties are projected onto the CFD-cell using the divided scheme (CFDEMcoupling documentation, 2016a; Norouzi et al., 2016). When using the divided scheme, each particle's volume is partitioned into 29 non-overlapping regions of equal volume. Subsequently, the solid fraction of each single CFD-cell is calculated via summation of the regions whose centroids are enclosed within the respective cell.

Similar to Eq. (1), the extinction coefficient represents the complete attenuation, both by absorption and by scattering:

$$\beta_p = \kappa_p + \sigma_p. \tag{8}$$

2.1.2.1. Dependent scattering.

We note in passing that the term $\frac{1}{1-\varphi_p}$ in Eq. (7) was introduced by Brewster (Brewster, 2004) to model the effect of surrounding particles on the radiative field (i.e., the so-called dependent scattering or shadowing (Tien & Drolen, 1987)). The term stems from the exact estimations of the mean penetration distance of a photon in packings of spheres.

2.1.2.2. Coarse-graining.

In the case of coarse-graining, Eq. (7) reads:

$$\langle \beta_p, \sigma_p, \kappa_p \rangle = \frac{1}{(1-\varphi_p)V} \sum_{i=1}^{N_{CG}} \varphi_{CG}^3 \langle Q_{ext,i}, Q_{sca,i}, Q_{abs,i} \rangle \left(\frac{d_{CG,i}}{\varphi_{CG}} \right)^2 \frac{\pi}{4}, \tag{9}$$

with N_{CG} being the number of parcels within the considered volume V, d_{CG} the parcel diameter, and $\varphi_{CG} = \frac{d_{CG}}{d_p}$ the particles' enlargement ratio.

2.2. P1 model formulation

The P1 model is the first order spherical harmonics approximation of the radiative transfer equation (Jeans, 1917; Modest, 2013). Generally, the radiative transfer equation is a function of spatial coordinates, angular coordinates, and wavelength. The P1 model eliminates the angular coordinates, while the gray body model assumption eliminates the wavelength dependency. The result is a diffusion-like conservation equation of the local incident radiation intensity G:

$$\nabla \cdot (\Gamma \nabla G) - \kappa G = -4\kappa_f \sigma T_f^4 - E_p. \tag{10}$$

In the equation above, Γ is the radiative diffusivity, κG is the intensity collectively absorbed by the particles and the fluid, $4\kappa_f \sigma T_f^4$ is the intensity emitted by the fluid, and E_p is the intensity emitted by the particles. The quantity σ is the Stefan-Boltzmann constant, and T_f is the temperature of the fluid. The emission contribution of the particles is evaluated at the computational cell volume V:

$$E_p = \frac{\sum_i^{N_p} Q_{abs,i} \pi d_{p,i}^2 \sigma T_{p,i}^4}{V(1-\varphi_p)}. \tag{11}$$

In the relation above, N_p is the number of the particles within the cell, $T_{p,i}$ is the i-th particle temperature, and φ_p is the local solid fraction, computed at the cell level from the particle position and size using the divided scheme (CFDEMcoupling documentation, 2016a; Norouzi et al., 2016).

The radiative diffusivity is defined as:

$$\Gamma = \frac{1}{3\kappa + \sigma_{eff}}, \tag{12}$$

where κ and σ_{eff} are respectively the absorption coefficient according to Eq. (5), and the effective scattering coefficient according to Eq. (6).

At the emitting walls, Marshak's boundary condition (Marshak, 1947) is imposed:

$$-\frac{2\Gamma(2-\varepsilon_w)}{\varepsilon_w}\hat{\mathbf{n}}\cdot\nabla G + G = 4\sigma T_w^4, \tag{13}$$

with ε_w being the emissivity of the wall, $\hat{\mathbf{n}}$ the unit normal vector of the wall, and T_w the wall temperature.

Alternatively, if the amount of radiative heat flux coming from a boundary ($|\mathbf{q}_{rad,b}|$) is known, the gradient of the incident radiation intensity is prescribed according to:

$$\nabla G = -\frac{|\mathbf{q}_{rad,b}|}{\Gamma}. \tag{14}$$

The heating rate due to radiation, experienced by a single particle, is the difference between the intensity that is absorbed: $Q_{abs}G_i/(1-\varphi_{p,i})$, and the intensity that is emitted: $4\sigma Q_{abs}T_{p,i}^4/(1-\varphi_{p,i})$, through the particle surface $\pi d_{p,i}^2/4$:

$$\dot{Q}_{rad,i} = \frac{Q_{abs}}{1-\varphi_{p,i}}\frac{\pi d_{p,i}^2}{4}\left(G_i - 4\sigma T_{p,i}^4\right). \tag{15}$$

Subscript i denotes that the solid fraction $\varphi_{p,i}$ and the incident radiation intensity G_i are interpolated to the particle location from continuum fields (i.e., the CFD-mesh). Division by $(1-\varphi_{p,i})$ takes the surrounding particles into account (see section 2.1.2).

Similarly, the radiation contribution to specific fluid enthalpy equation is:

$$S_{rad} = \kappa_f\left(G - 4\sigma T_f^4\right). \tag{16}$$

To improve the numerical stability, the above term is typically split into explicit and implicit contribution (Patankar, 1980). Details on the corresponding computational procedure are provided for example in (Cintolesi et al., 2017). Since we encounter only transparent fluids in our present study, the above term is zero, and does not affect the computational procedure.

Once the radiative intensity is known, the radiative heat flux is evaluated from:

$$\mathbf{q}_{rad} = -\Gamma\nabla G. \tag{17}$$

The relation above could also be injected in Eqs. (10) and (13). This would form a system of two 1st-order partial differential equations for the incident radiation and the radiative heat flux. Such a formulation (although preferred for radiative equilibrium in a gray medium (Modest, 2013)) is not compatible with the finite volume method used in CFD. Moreover, most CFD codes are interested only in the heat flux that comes to the surfaces of the enclosure, evaluating Eq. (17) only at the boundaries of the domain (e.g. (Cintolesi et al., 2017)). Here, we calculate the radiative heat flux over the entire domain, since it is of interest how the radiative heat flux varies over the particle bed. The next section details the numerical strategies employed for diminishing oscillations in the heat flux solution.

2.3. Handling of heat flux oscillations

P1 model is expected to lose accuracy if radiative properties are non-uniform (Dombrovsky, 1997; Dombrovsky, 2010; Modest, 2013; Viskanta & Mengüç, 1987). Most gas-particle applications, such as fluidized beds and rotary kilns, feature non-uniformity due to spatial fluctuations of the particle concentration.

Radiative heat transfer equation predicts temperature jumps at discontinuities (Heaslet & Warming, 1965), which the P1 model, being a 1st order approximation, cannot resolve. Instead, we observe unphysical heat flux oscillations near sharp gradients in the solid fraction field (see subsection 3.3).

Several measures are taken to reduce the influence of these sharp gradients on the solution.

First, a harmonic interpolation from cell centres to cell faces (Moukalled et al., 2016) is enforced for the radiative diffusivity (Eq. (12)).

Second, to avoid the diffusivity tending to infinity in the case of a cell completely void of particles, we add the fluid scattering contribution in Eq. (6). The value for the fluid scattering coefficient is set to $\sigma_f = 1.23 \times 10^{-5}\ \mathrm{m}^{-1}$. This is the scattering coefficient of the atmosphere, responsible for the blue color of the sky (Penndorf, 1957).

Third, the radiative heat flux from Eq. (17) is re-written by exploiting the differentiation product rule, arriving at:

$$\mathbf{q}_{rad} = G\nabla\Gamma - \nabla(\Gamma G). \tag{18}$$

While the aforementioned measures improve the numerical solution, a certain amount of heat flux oscillations is mathematically bound to occur. This becomes a large issue even for densely packed beds if the computational cells are small compared to the particle size. As demonstrated in subsection 3.2.3, such cases can lead to heat flux oscillations as extreme as 10^8%.

These extreme oscillations can be removed by artificially reducing discontinuities in radiative properties. Specifically, we suggest two correction strategies: 1) smoothing of the radiative diffusion field, and 2) pseudo-scattering of the fluid.

Smoothing is a procedure of redistributing values over a length L_{smooth} in order to achieve a more uniform field. The procedure is today routinely applied to void fraction and momentum-exchange fields in CFD-DEM simulations, as detailed in (Capecelatro & Desjardins, 2013; Pirker et al., 2011; Radl et al., 2014). Here, we apply smoothing to the radiative diffusivity field Γ by solving:

$$\frac{\partial\Gamma}{\partial t} = D\nabla^2\Gamma, \tag{19}$$

where the diffusion coefficient is:

$$D = \frac{L_{smooth}^2}{\Delta t}. \tag{20}$$

Alternatively, the variations of the radiative diffusivity field might be ameliorated by introducing pseudo-scattering of the fluid to Eq. (6):

$$\sigma_{eff} = (1-\varphi_p)\varsigma_f + \sigma_p(3-A_1). \tag{21}$$

According to above, cells devoid of particles will have attenuation properties proportional to ς_f. If ς_f is selected as a small fraction of the overall extinction coefficient (i.e., $5\%\beta \leq \varsigma_f \leq 20\%\beta$), the difference between the gas-filled and the particle-filled cells will be reduced, while keeping the increase of the overall opacity negligible.

3. Results

3.1. Optical thickness of granular media

The optical thickness, defined as:

$$\tau_L = \int_0^L \beta(x)\mathrm{d}x, \tag{22}$$

describes the degree of transparency of a system to radiation. For a medium with uniform properties, the optical thickness (or opacity) along the path L reduces to:

$$\tau_L = \beta L. \tag{23}$$

In such a medium, the extinction coefficient β is the inverse of the mean penetration distance (Howell et al., 2010):

$$l_m = \frac{1}{\beta}. \tag{24}$$

The mean penetration distance is the average distance a photon can reach in a medium without being absorbed or scattered away. This physical quantity is similar to the mean free path of a molecule. In a vacuum, the extinction coefficient is zero, and the mean penetration distance tends to infinity. In contrast, for an infinitely large extinction coefficient, the mean penetration distance tends to zero, and the medium is completely opaque. Practically, e.g. solid metals are considered completely opaque, with a typical mean penetration distance of 10 nm to 1 μm (Tolochko et al., 2000).

Systems are classified as optically thin if $\tau_L \ll 1$, or as optically thick if $\tau_L \gg 1$. Based on comparisons with other methods, P1 model is reported as being accurate for large opacities, i.e., $\tau_L > 2$ (Viskanta & Mengüç, 1987). In that case, all incident radiation is attenuated locally, eliminating the directional dependency at the enclosure scale. Already at $\tau_L = 10$, according to the Beer–Bouguer–Lambert law (Howell et al., 2010), 99.995% of energy is attenuated within the medium, making it effectively opaque.

Most granular media fall into the optically thick category, as seen in Fig. 1. Combining Eqs. (7) and (23) for a monodispersion of large spheres ($Q_{ext} = 1$), we obtain the relationship between the optical thickness τ_L, and the system parameters including solid fraction φ_p, particle diameter d_p, and enclosure length L (we note in passing that the absorptivity of the particles does not influence the optical thickness).

As seen in Fig. 1, a dilute system with $\varphi_p = 0.1$ requires a length of only 10 particle diameters to comprise an optically thick medium, and 60 particle diameters for an opaque medium. In a densely packed system, with $\varphi_p = 0.5$, the opaqueness limit is reached already at 6 particle diameters. This – alongside recent insights from Monte Carlo simulations of radiation in randomly packed beds of spheres (Liu et al., 2021) – suggests that the P1 model is suitable for describing radiative heat transfer in granular media.

3.2. Equilibrium heat flux and temperature distribution

To verify our P1 implementation, we use the exact solution for a radiative equilibrium in a gray medium between two isothermal black plates from Heaslet and Warming (Heaslet & Warming, 1965). This solution is well-known in literature: for example, it was already used to benchmark the P1 implementation in OpenFOAM for a gray gas (Cintolesi et al., 2017), and it was used to validate the Monte Carlo ray tracing method for polydisperse particles (Chen et al., 2022) – albeit without details provided on the specific validation case setup.

Still, repeating the same benchmark is necessary here, as our implementation differs in a few details, most notably in the way the heat flux is treated. In the formulation intended for fluid calculations, the radiative heat flux is usually defined only at the wall boundaries of the domain, as it is the case in (Cintolesi et al., 2017). We, however, compute the heat flux over the entire domain. As detailed in subsection 2.3, the heat flux is prone to both numerical and model errors if applied to a non-uniform medium.

Another departure from the standard P1 implementation is the addition of Brewster's correction to model dependent scattering (see Eq. (7)). This inclusion alters the extinction efficiency of granular media and also alters the transient behaviour.

3.2.1. Test case setup

We consider three situations, as depicted in Fig. 2: (a) a uniform packing of monodisperse spheres, (b) a uniform packing of bidisperse spheres, and (c) a random packing of polydisperse spheres.

Relevant simulation parameters are given in Table 2. At the emitting walls, Marshak's boundary condition is imposed (Eq. (13)). Cyclic boundary condition is imposed elsewhere. The fluid

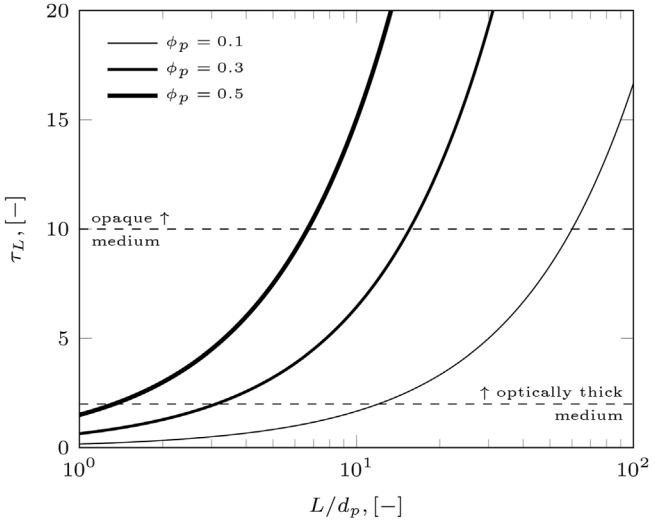

Fig. 1. Optical thickness in packed beds of large particles with $Q_{ext} = 1$.

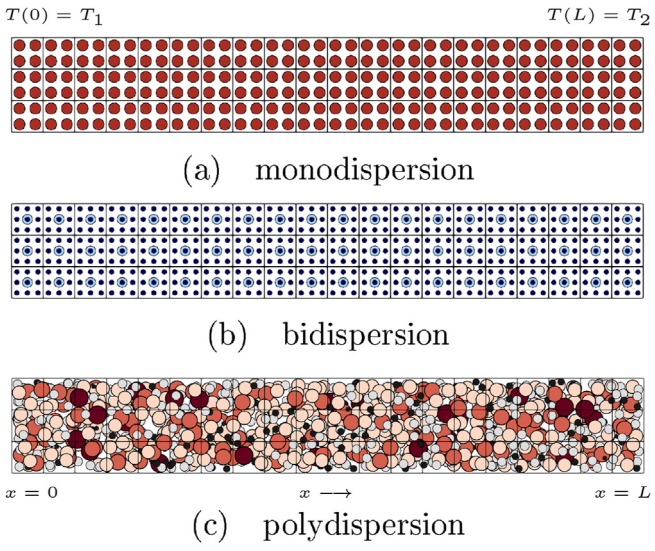

Fig. 2. Simulation domain for steady-state simulations.

temperature is set to 273.15 K. As the fluid is non-absorbing (only slight scattering is allowed, as discussed in subsection 2.3) and convective heat transfer is excluded, the fluid temperature remains constant and is hence unaffected by thermal radiation. The fluid velocity is set to no-slip at the hot wall, and to zero gradient at the cold wall. The pressure is set to 1 bar at the cold wall, and to zero gradient at the hot wall. Drag is calculated according to the closure of Koch-Hill (Koch & Hill, 2001), but since the particles are fixed, no signification variations of the flow field are observed. The void fraction is mapped from particle positions according to the divided scheme (CFDEMcoupling documentation, 2016a; Norouzi et al., 2016).

Test case-specific particle properties are given in Table 3. Size distribution for the polydisperse case is shown in Fig. 3. In all cases, particles are given a uniform extinction efficiency, stemming from Eq. (7) and the prescribed optical thickness according to Eq. (23). Contributions to extinction from absorption and scattering are considered equal, i.e., $Q_{abs} = Q_{sca} = 0.5$, with the scattering being isotropic (i.e., $A_1 = 0$). However, as demonstrated in Appendix B, the ratio of absorption and scattering affects only the transience, and does not influence the steady-state results presented in this section.

The uniform particle packing used in the monodisperse and the bidisperse setup ensures equal solid fraction distribution in CFD cells. However, continuum-based models are generally not applicable to regular arrangements of particles (Li & Chandran, 2022; Liu et al., 2021), due to the ray transmission through the interstitial spaces. On the other hand, random arrangements diffuse the heat transport by enforcing multiple scatterings and absorptions. Paradoxically, as discussed before in subsection 2.3, spatial variations, i.e., inhomogeneities in the domain, tend to cause calculation errors (Dombrovsky, 1997; Dombrovsky, 2010; Modest, 2013; Viskanta & Mengüç, 1987).

3.2.2. Temperature distribution

The equilibrium emissive power (i.e., the normalized temperature) for a gas-particle system of various opacities is shown in Fig. 4.

Table 2
Simulation parameters.

Parameter	Value
hot wall temperature	$T_1 = 1000$ K
cold wall temperature	$T_2 = 500$ K
wall emissivity	$\varepsilon_{w1} = \varepsilon_{w2} = 1$
domain length	$L = 0.02$ m
number of cells	$3 \times 3 \times 20$
initial particle temperature	$T_{p,0} = 300$ K
particle density	$\rho_p = 1000 \frac{\text{kg}}{\text{m}^3}$
particle heat capacity	$c_p = 10000 \frac{\text{J}}{\text{kgK}}$

Table 3
Particle properties.

	Monodispersion	Bidispersion	Polydispersion
N_p	1440	4860	1000
d_p	375 μm	167 μm, 333 μm	375 μm*
φ_p	0.221	0.082	0.194
Q_{ext}/β	0.00088177	0.0014020	0.0012086

*mean, see Fig. 3.

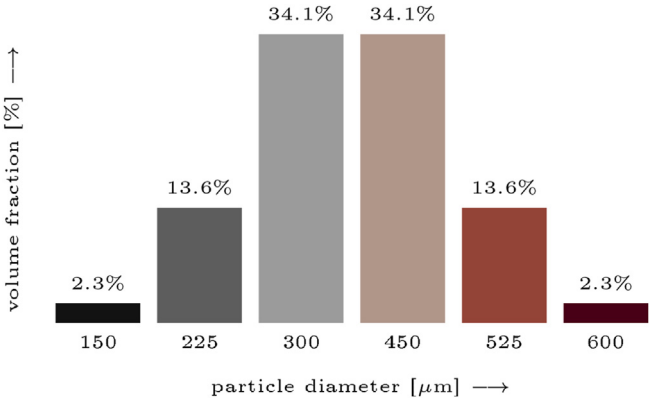

Fig. 3. Volumetric size distribution in polydispersion.

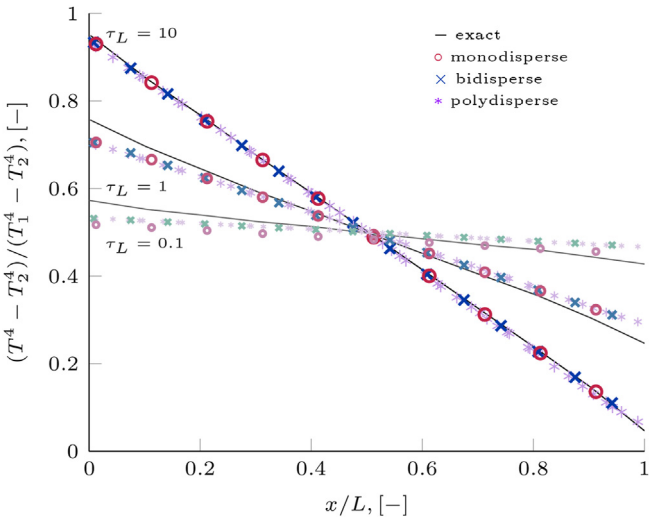

Fig. 4. Emissive power established in granular media (setup from Table 3).

Based on comparisons with other methods, the P1 model is expected to show excellent agreement for optically thick media, with $\tau_L \gg 1$. Our results confirm this, as for an opacity of $\tau_L = 10$ almost perfect agreement is achieved. In this case, the emissive power changes linearly with the normalized location between the hot and the cold boundary, according to the following approximate relation (Heaslet & Warming, 1965):

$$\varphi = \frac{T(\tau)^4 - T_2^4}{T_1^4 - T_2^4} \approx \left[\frac{-\frac{3}{4}(\tau - \tau_L) + \frac{1}{\varepsilon_{w2}} - \frac{1}{2}}{\frac{1}{\varepsilon_{w1}} + \frac{1}{\varepsilon_{w2}} - 1 + \frac{3}{4}\tau_L} \right]_{\tau_L \gg 1} . \tag{25}$$

However, as the case is one-dimensional and isotropic, good agreement is achieved also at lower opacities. The greatest departure is observed at the boundaries, where non-linear effects are dominant. However, the discrepancy does not exceed approximately 10%. Having in mind that the emissive power is proportional to the 4th power of temperature, the associated temperature error is at least four times smaller:

$$\frac{(\varphi+\delta_\varphi)-\varphi}{\varphi}=\frac{(T+\delta_T)^4-T^4}{T^4},$$
$$\frac{\delta_\varphi}{\varphi}=\frac{(T^4+4\delta_T T^3+6\delta_T^2T^2+4\delta_T^3T+\delta_T^4)-T^4}{T^4}, \quad (26)$$
$$\Delta_\varphi=4\Delta_T+6\Delta_T^2+4\Delta_T^3+\Delta_T^4\approx 4\Delta_T.$$

In the relation above, δ is the absolute and Δ the relative error. According to Eq. (15), at the equilibrium, the incident intensity G is also proportional to the 4th power of the temperature, holding the same relative error relationship. Illustrated in Fig. 5, error as large as 20% in incident radiation leads to only 5% error in temperature. Thus, we next consider the heat flux as a more sensitive measure of the computational precision.

3.2.3. Equilibrium radiative heat flux

The mean dimensionless heat flux (average across the domain) for various opacities is shown in Fig. 6 against the exact solution (Heaslet & Warming, 1965):

$$\psi_b=\frac{q_i}{\sigma\left(T_1^4-T_2^4\right)}=\left[\frac{4/3}{1.42089+\tau_L}\right]_{\tau_L\gg 1}. \quad (27)$$

The dimensionless heat flux above is valid for radiative equilibrium established between black walls (i.e., $\varepsilon_{w1}=\varepsilon_{w2}=1$). We note in passing also the dimensionless equilibrium heat flux for gray walls (Heaslet & Warming, 1965; Modest, 2013):

$$\psi=\frac{q_i}{\sigma\left(T_1^4-T_2^4\right)}=\frac{\psi_b}{1+\psi_b\left(\frac{1}{\varepsilon_{w1}}+\frac{1}{\varepsilon_{w2}}-2\right)}. \quad (28)$$

Even though the mean heat flux agrees well with the exact solution in the whole range of opacities, variation of the local cell values is observed. This is especially pronounced for the polydisperse packing, where the void fraction, and therefore radiative properties, vary from cell to cell. If the size of the computational cell drops below the average particle diameter, the extreme local heat flux oscillations also affect the mean heat flux.

As seen in Fig. 7, for the polydisperse packing at $\tau_L=10$, the error in the mean heat flux jumped at over 10^8% when the number of cells per length increased ($N_L\geq 50$). These extreme oscillations are completely removed by smoothing (CFDEMcoupling documentation, 2016b). In contrast, the error due to small cell size (i.e., large N_L), even though reduced, is still too large after correction with pseudo-scattering. The temperature solution retained high precision (less than 10% discrepancy from Eq. (25)) for all correction procedures.

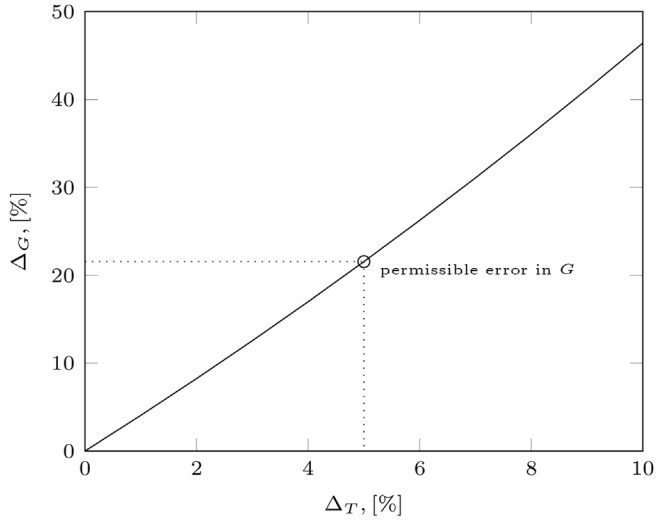

Fig. 5. Relationship between relative errors in temperature and incident radiation intensity.

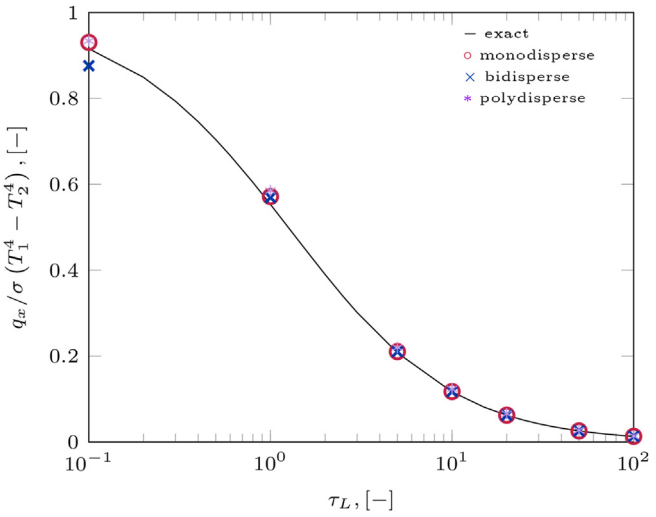

Fig. 6. Equilibrium mean heat flux in a particle bed (setup from Table 3).

Even with correction procedures employed, there is a dispersion of local heat flux values: Fig. 8 shows the coefficient of variance (ratio of the standard deviation and the mean value) for the radiative diffusivity and the heat flux.

While smoothing certainly outperforms pseudo-scattering according to the data shown here, pseudo-scattering is still useful for cases with a small number of particles (e.g. as in subsection 3.4.1), since large smoothing lengths may cause unbounded temperatures.

3.2.4. Verification of coarse-graining

To verify the coarse-graining implementation, we compare the simulation results to the exact solution from Heaslet and Warming (Heaslet & Warming, 1965). The simulation setup remains the same as described previously, with parameters detailed in Table 2. Again, we use the three cases depicted in Fig. 2: (a) a uniformly packed monodispersion, (b) a uniformly packed bidispersion, and (c) a randomly packed polydispersion.

Particle parameters are as defined in Table 3 with one important exception: the assigned extinction efficiency Q_{ext} is divided by the particles' enlargement ratio $\varphi_{CG}=d_{CG}/d_p$. This allows the same geometrical setup to represent different levels of coarse-graining.

The resulting emissive power achieved with coarse-graining of $\varphi_{CG}=1000$ and $\varphi_{CG}=1\,000\,000$ is shown in Fig. 9 for an opacity of $\tau_L=10$.

The results agree extremely well, with no discernible difference in data obtained with and without coarse-graining. Monodisperse, bidisperse, and polydisperse systems all retained their precision in temperature, heat flux, and time, as described in previous sections.

This demonstrates practically limitless applicability of coarse-graining with P1, given that the system is self-similar (i.e., identical solid fraction distribution in each computational cell). However, and as mentioned, in practice particle coarse-graining may typically result in parcels being larger than a computational cell. This again stresses the importance for smoothing of the particle volume fraction field to ensure particle coarse graining yields realistic results.

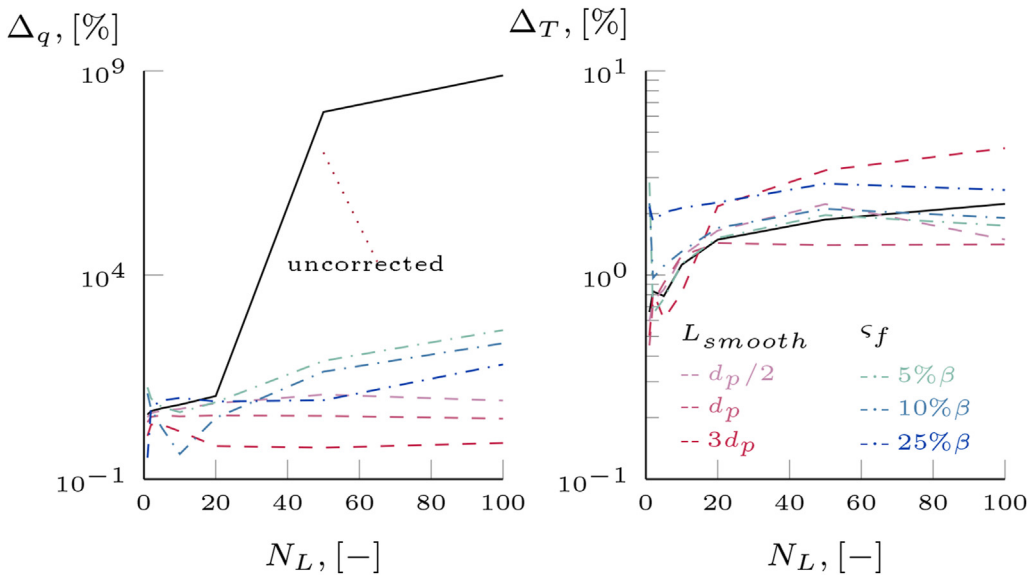

Fig. 7. Relative error in the mean heat flux Δ_q and temperature Δ_T for polydispersion with $\tau_L = 10$ versus number of cells per length N_L.

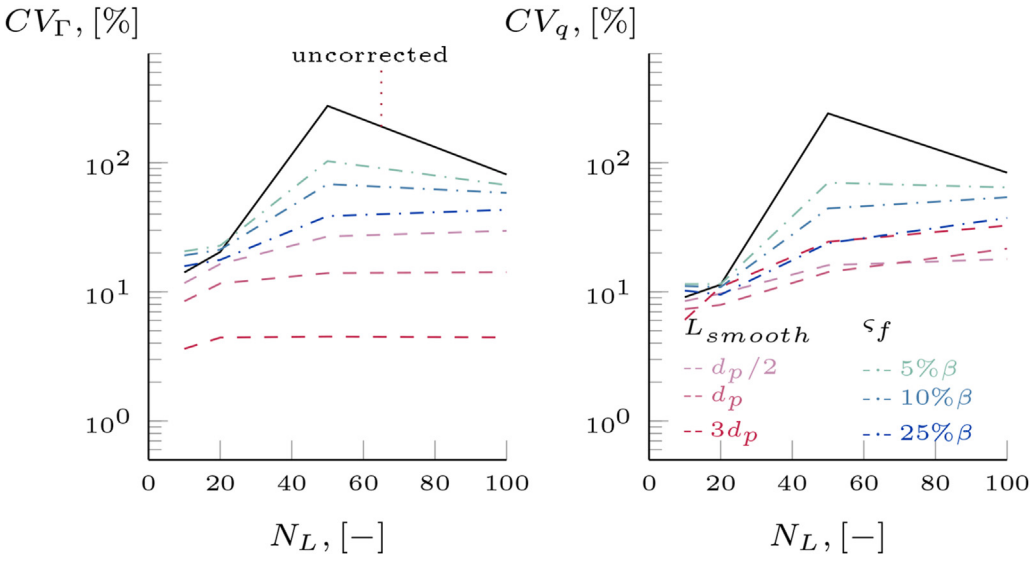

Fig. 8. Coefficient of variation in the radiative diffusivity CV_Γ and the heat flux CV_q versus number of cells per length N_L.

3.3. The effect of packing heterogeneity on the solution

The P1 model is reported to lose accuracy in a non-uniform medium (Dombrovsky, 1997; Dombrovsky, 2010; Modest, 2013; Viskanta & Mengüç, 1987). In order to quantify the degree of the tolerable non-uniformity, we analytically derive approximate relations for the equilibrium-state in a packed bed with a step change in opacity. While this setup is very simple, it has the advantage that we are able to derive an approximate solution for it, based on the exact solution given by Heaslet and Warming (Heaslet & Warming, 1965).

As seen in Fig. 10, we construct such a bed from two uniform monodisperse regions, each with identical number of particles, but of a different diameter. As a result, each region has a different void fraction and a different opacity.

According to Eq. (22), the total opacity of the bed is found by summing up the opacities of the two involved regions:

$$\tau_L = \beta_1 L_1 + \beta_2 L_2 = \tau_{L1} + \tau_{L2}. \tag{29}$$

In thermal equilibrium, the heat flux is constant along the bed length:

$$\psi\left(T_1^4 - T_2^4\right) = \psi_1\left(T_1^4 - T_{1i}^4\right) = \psi_2\left(T_{i2}^4 - T_2^4\right). \tag{30}$$

Assuming both regions of the bed are optically thick (τ_{L1}, $\tau_{L2} \gg 1$), the normalized heat fluxes (ψ, ψ_1 and ψ_2) stem from Eq. (27) (Heaslet & Warming, 1965). Temperatures T_{1i} and T_{2i}, which denote respectively the left- and the right-hand side of the interface, follow from:

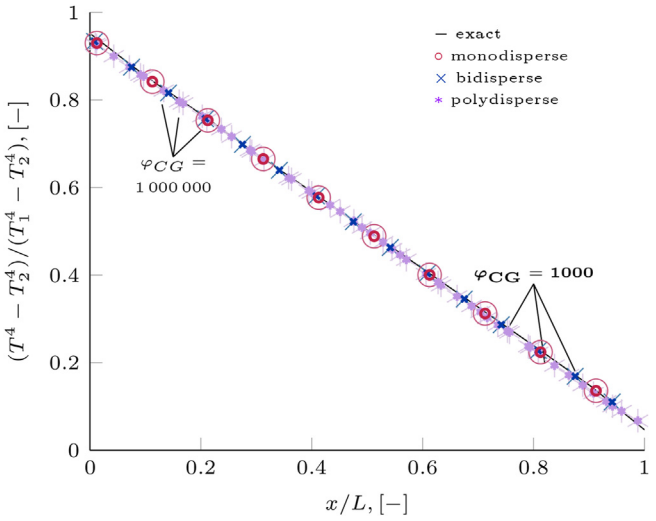

Fig. 9. Influence of coarse-graining on the emissive power in granular media with opacity $\tau_L = 10$ (setup adapted Table 3).

$$\begin{aligned} T_{1i}^4 &= T_1^4 - \frac{\psi}{\psi_1}\left(T_1^4 - T_2^4\right), \\ T_{i2}^4 &= T_2^4 + \frac{\psi}{\psi_2}\left(T_1^4 - T_2^4\right). \end{aligned} \tag{31}$$

It is easily shown that there is a temperature jump at the interface, such that $T_{i2} > T_{1i}$. From Eq. (31), it follows that:

$$T_{1i}^4 - T_{i2}^4 = \left(T_1^4 - T_2^4\right)\left[1 - \psi\frac{\psi_1 + \psi_2}{\psi_1\psi_2}\right]. \tag{32}$$

The term containing the normalized heat fluxes can be expanded using Eqs. (27) and (29) into:

$$\psi\cdot\frac{\psi_1 + \psi_2}{\psi_1\psi_2} = \frac{A}{B + \tau_L}\cdot\frac{\frac{A}{B+\tau_{L1}} + \frac{A}{B+\tau_{L2}}}{\frac{A}{B+\tau_{L1}}\cdot\frac{A}{B+\tau_{L2}}} = \frac{2B + \tau_L}{B + \tau_L} > 1, \tag{33}$$

where constants $A = 3/4$ and $B = 1.42089$ are introduced to simplify the expression. Returning to Eq. (32), since $\left(T_1^4 - T_2^4\right) > 1$ and $\left(1 - \frac{2B+\tau_L}{B+\tau_L}\right) < 1$, also $\left(T_{1i}^4 - T_{i2}^4\right) < 1$ must be true.

In other words, the interface temperature facing the cold boundary is greater than the interface temperature facing the hot boundary.

Temperature discontinuities are expected in radiative heat transfer. Remembering the exact solution by Heaslet and Warming (Heaslet & Warming, 1965), a temperature slip was found next to the wall boundary (see Fig. 4).

In a real-world granular medium, there is no sharp interface separating densely packed and dilute regions, and therefore the temperature distribution should be smooth.

However, when applying a continuum-based radiation model, temperature jumps are mathematically imposed. Being a low-order approximation, the P1 model is not able to fully resolve the discontinuity and predicts an interface temperature between T_{1i} and T_{i2}. As a consequence, heat flux oscillations arise.

To showcase these oscillations, we use a domain as shown in Fig. 10. The overall opacity is set to $\tau_L = 50$, while opacities of the regions are varied according to Table 4. The rest of the simulation parameters remained as shown in Table 2, with the exception of the domain length L which is here extended to 0.1 m. The two regions of the bed each occupy half of the domain: $L_1 = L_2 = L/2$, and the diameter of the bigger particle is set to 0.4 mm.

The resulting temperature and emissive power are shown in Fig. 11, and the heat flux (sampled along the bed length) is shown in Fig. 12.

While the interface temperature settles between the predicted limiting values from Eq. (31), heat flux responds with an oscillation. The oscillation is proportional to the change in properties: relative errors of 53%, 15%, and 5% compared to Eq. (27) correspond to particle diameter change of 50%, 25%, and 10%, respectively.

To achieve the displayed results, a fine mesh with $N_L = 200$ was needed. As seen in Fig. 13, coarser meshes lead to higher maximum heat fluxes, as well as larger departures from the average interface temperature $(T_{1i} + T_{i2})/2$.

In the future, a more complex setup for a non-uniform particle distribution (e.g., with a fixed gradient) should be investigated, ideally considering a (semi-)analytical solution as a reference.

3.4. Validation of the radiation model

In this section, we validate our code with experimental measurements of heat transfer quantities in a pebble bed. First, in subsection 3.4.1, we consider vacuum conditions, involving heat

Table 4
Parameters used in simulations of a bed with a step change in opacity.

d_{p1}/d_{p2}	Q_{ext}	β_1	β_2	Γ_1/Γ_2
0.5	6.1216	159.19	840.81	5.28
0.75	4.9723	317.03	682.96	2.15
0.9	4.1918	424.25	575.75	1.35
1.11	4.1918	575.75	424.25	0.74
1.33	4.9723	682.96	317.03	0.46
2	6.1216	840.81	159.19	0.18

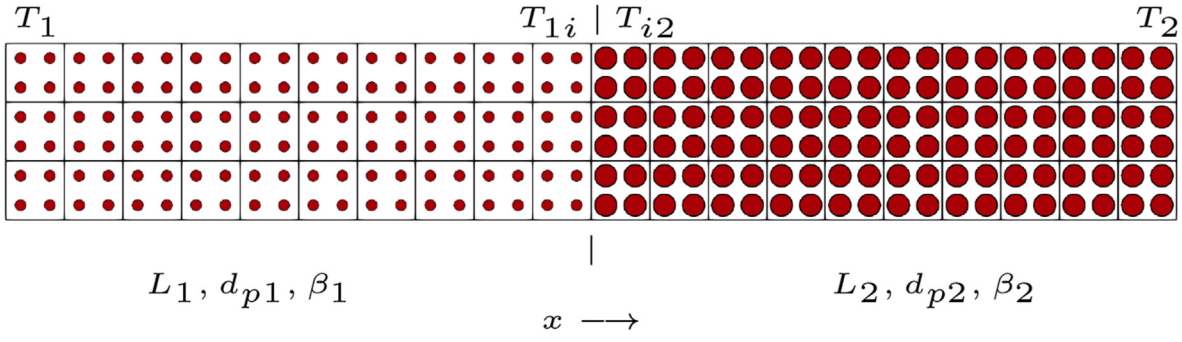

Fig. 10. Packed bed with a step change in opacity.

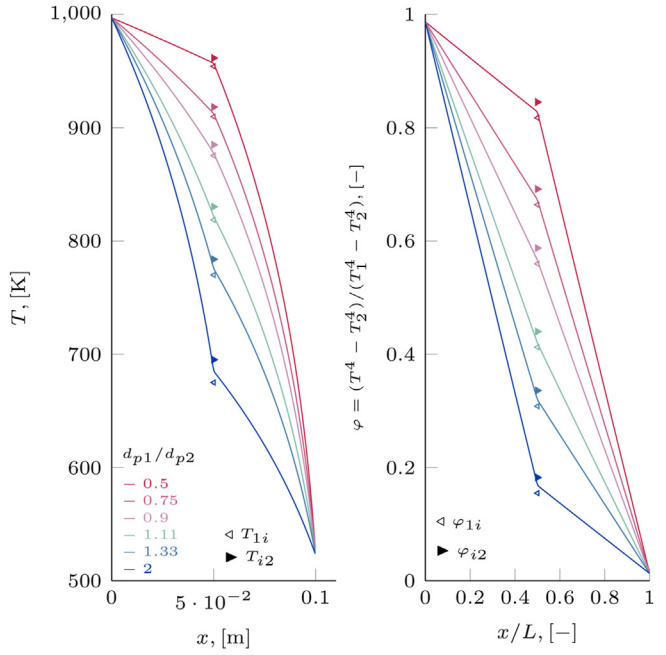

Fig. 11. Temperature distribution (left) and emissive power (right) established in a packed bed with a step change in solid fraction (setup from Table 4). Solid lines refer to the numerical solution; left and right triangles represent analytically obtained temperatures at the left and right side of the interface.

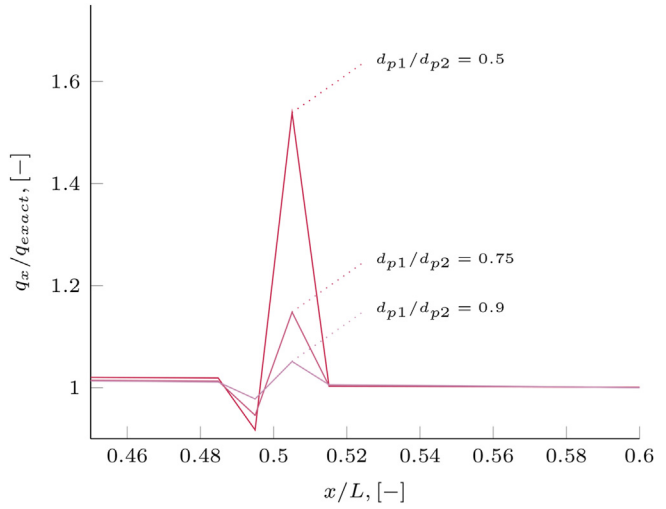

Fig. 12. Heat flux per length of a packed bed with a step change in solid fraction (setup from Table 4).

transfer via radiation and conduction at the pebble contacts. Our results are compared to predictions of a view-factor–based model (Tausendschön & Radl, 2021) and to experimental data (De Beer, 2014). Second, in subsection 3.4.2, we consider also the influence of an interstitial gas using the experimental data from the SANA test facility (Stöcker & Niessen, 1997).

3.4.1. Pebble bed under vacuum conditions

Here, we recreate a pebble bed under vacuum conditions, as studied experimentally by De Beer (De Beer, 2014). The experimental setup involves about 300 pebbles placed between a heated, and a cooled reflector wall. Measured quantities include the steady-state temperature profile and the steady-state heat flux.

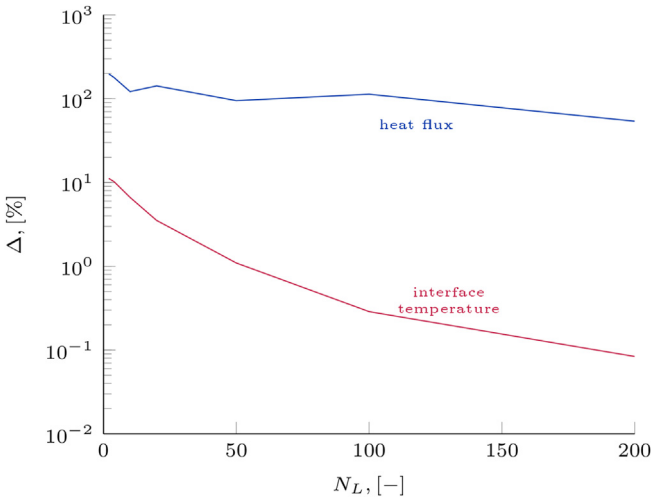

Fig. 13. Relative error in maximum heat flux and interface temperature for a bed with a step change in opacity (case $d_{p1}/d_{p2} = 0.5$ from Table 4).

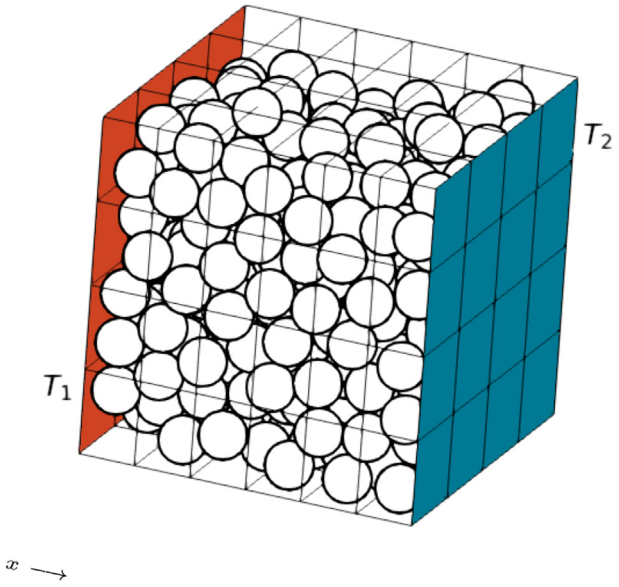

Fig. 14. Pebble bed under vacuum—simulation domain.

The simulation domain is shown in Fig. 14. Pebbles and reflector walls are graphite, with a temperature sensitive heat conductivity (De Beer, 2014). We interpret the setup as one-dimensional, excluding the influence of non-graphite boundaries. Hot and cold wall boundaries are isothermal. Remaining simulation parameters are summarized in Table 5.

3.4.1.1. Radiative heat transfer. We start by examining the radiation-only solution (no conductive heat transport). We first briefly discuss (data not shown) the influence of simulation parameters such as mesh resolution, strategies for removal of heat flux oscillations, and the closure for dependent scattering. Next, we compare our results to the view-factor–based predictions given by Tausendschön and Radl (Tausendschön & Radl, 2021). Since the setup is one-dimensional (similar to subsection 3.2), we also consider the analytic solution (Heaslet & Warming, 1965).

Table 5
Pebble bed under vacuum—simulation parameters.

Parameter	Value
particle diameter	$d_p = 0.06$ m
domain size	0.42 m × 0.42 m × 0.42 m
number of particles	332
particle density	$\rho_p = 1650 \frac{\text{kg}}{\text{m}^3}$
Young's modulus for heat transfer	$Y_{orig} = 11 \times 10^9$ Pa
Young's modulus for bed creation	$Y = 5 \times 10^8$ Pa
particle heat capacity	$c_p = 710 \frac{\text{J}}{\text{kgK}}$
particle absorption efficiency	$Q_{abs} = 0.8$
particle scattering efficiency	$Q_{sca} = 0.2$
reflector wall emissivity	$\varepsilon_w = 0.8$
simulation time step	$\Delta t = 1$ s
400 °C	
inner reflector temperature	$T_1 = 673.15$ K
outer reflector temperature	$T_2 = 332.54$ K
800 °C	
inner reflector temperature	$T_1 = 1073.15$ K
outer reflector temperature	$T_2 = 436.5$ K

3.4.1.2. Influence of mesh resolution. The small length of the domain (7 particle diameters) limits the choice of the mesh resolution. Meshes of 4, 6, and 8 cells per length yield less than 10% relative difference for the temperature solution. However, all meshes produce a large dispersion of the equilibrium radiative heat flux. Least dispersion, attained for the coarse mesh with 4 cells per length, results in a coefficient of variation of 20% (i.e., ratio of the standard deviation and the mean value). Finer meshes, with 6 and 8 cells per length, both have cells devoid of particles, and therefore heat flux oscillations in the scale of 10^6 and more are observed. While both smoothing and pseudo-scattering are able to remove these large oscillations, unfortunately neither technique eliminates the dispersion.

3.4.1.3. Influence of smoothing and pseudo-scattering. Smoothing with $L_{smooth} = L_{cell}/2$ and $L_{smooth} = L_{cell}$ applied to the mesh with 8 cells per length, yields a coefficient of variation in heat flux of respectively 55% and 38%. For the coarse mesh, with 4 cells per length, the coefficient of variation remains around 20% after smoothing with $L_{cell}/2$, and increases to 35% for L_{cell}. Moreover, smoothing adversely affects the temperature, introducing up to 20% difference for all meshes.

On the other hand, the temperature remains unaffected by pseudo-scattering, with less than 1.5% difference. For the coarse mesh with 4 cells, a pseudo-scattering coefficient of 5 m^{-1} (i.e., 20% of the extinction coefficient) is needed to reduce the coefficient of variation to 19%. The same amount of pseudo-scattering yields 28% variation coefficient for mesh with 8 cells per length.

3.4.1.4. Influence of dependent scattering. Influence of the closure for dependent scattering is tested for the 800 °C-case. While the effect on the resulting temperature profile is only slight (around

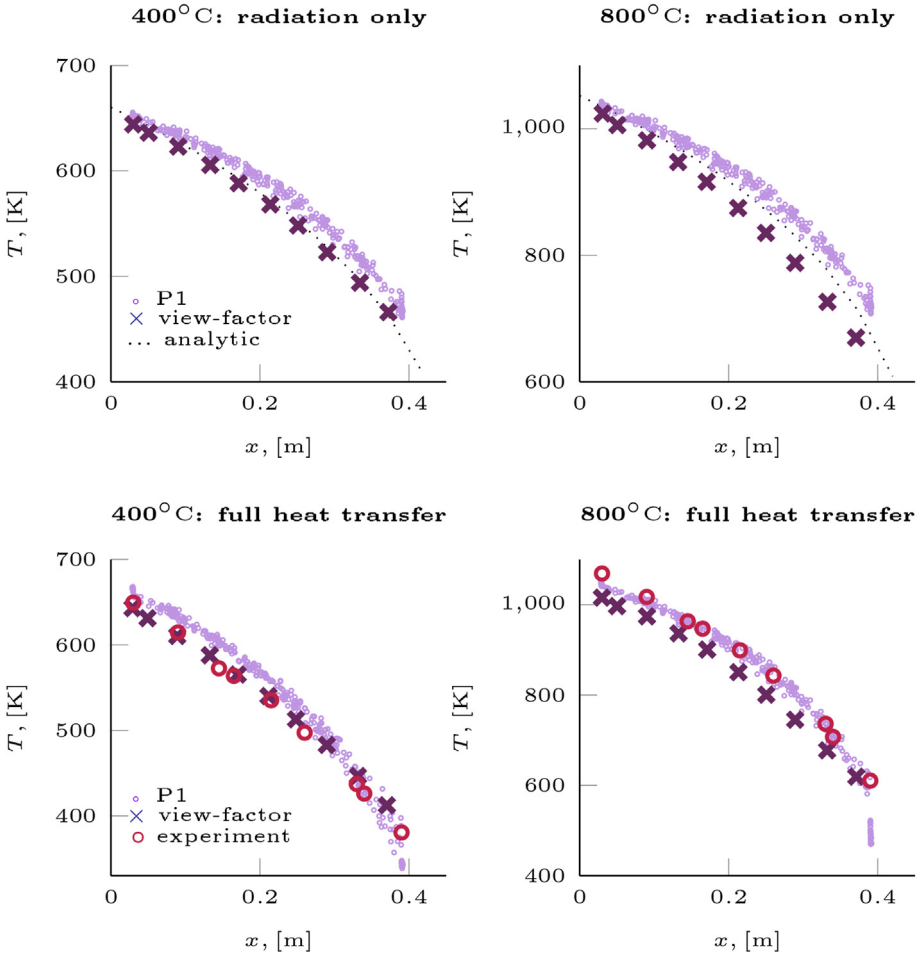

Fig. 15. Steady-state temperature distribution established in a pebble bed under vacuum (setup from Table 5).

Table 6
Equilibrium heat-flux $\left[\frac{W}{m^2}\right]$ for a pebble bed under vacuum (setup from Table 5).

Case	400°C radiation only	800°C radiation only	400°C full heat transfer	800°C full heat transfer
P1, total	–	–	2296	9419
P1, radiative	$1165^{\mu}(281^{\sigma})$	$7817^{\mu}(1771^{\sigma})$	$1232^{\mu}(392^{\sigma})$	$8150^{\mu}(2240^{\sigma})$
analytic (Heaslet & Warming, 1965)	1134	7583	–	–
view-factor (Tausendschöen & Radl, 2021)	806.9	5421	1654	6733
experimental (De Beer, 2014)	–	–	1629	9397
μ – mean, σ – standard deviation				

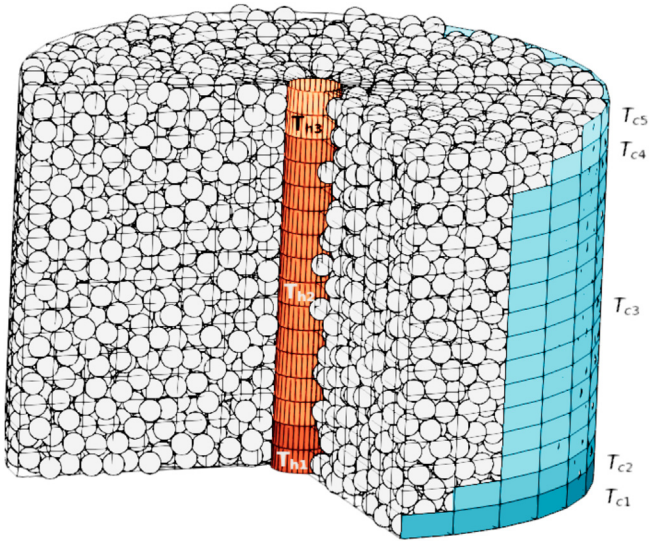

Fig. 16. Schematic of the simulation domain for the SANA test case.

1%), a simulation without depended scattering yields a 60% greater mean heat flux, and also takes 35% longer time to reach the steady state.

3.4.1.5. Temperature distribution and heat flux. The equilibrium temperature distribution shown in Fig. 15 (top, left and right) uses a mesh of 6 cells per length with a pseudo-scattering coefficient of 2.5 m^{-1} (i.e., 10% of the extinction coefficient).

Good agreement of our P1 model predictions is obtained with view-factor – based predictions (Tausendschöen & Radl, 2021): the mean relative difference is around 3% for the 400 °C-case, and around 6% for the 800 °C-case. Compared to the analytical solution (Eq. (25)), the mean difference stays around 3% for both cases.

Results for the equilibrium heat flux are summarized in Table 6. The relative difference of the mean heat flux compared to (Tausendschöen & Radl, 2021) is around 44% for both cases. Better agreement, with 3% relative difference, is achieved with the exact solution for a continuous gray medium (Eq. (28)) (Heaslet & Warming, 1965).

The discrepancy from the view-factor–based results suggests that continuum assumption adopted by us might not be valid in systems with small number of particles. The coefficient of variation remained at around 24% in both cases.

3.4.1.6. Full heat transfer. As the bed is under vacuum, only radiation and conduction within particles contribute to the heat transfer. A temperature-sensitive heat conductivity is taken from (De Beer, 2014). The contact area for conduction is corrected for the Young's modulus for graphite (Entegris, 2013).

Bottom left and right graph in Fig. 15 show the resulting temperature profile compared to the experimental measurements (De Beer, 2014) and the view-factor–based numerical predictions (Tausendschöen & Radl, 2021). Steady-state heat fluxes are given in Table 6.

Temperature profiles agree well with experimental data, with 4% precision at 400 °C, and 2% at 800 °C. Similarly, compared to the view-factor–based solution, the mean discrepancy in temperature is around 3% at 400 °C, and around 5% at 800 °C. It should be also highlighted here that the temperature profiles exhibit slip at the boundaries, most notable near the cold boundary in the radiation-only solution. Thus, even though the boundaries are set as isothermal, influence of radiation significantly affects the final state. Still, for such a case heat flux is a more relevant measure of accuracy.

The discrepancy of the total heat flux (i.e., the sum of the conductive and the mean radiative heat flux) is at about 40% compared to (Tausendschöen & Radl, 2021). The same discrepancy is found with the experimental data at 400 °C, which is expected since the view-factor–based solution was calibrated for this data point. However, the relative error for the heat flux at 800 °C is only 0.23%, while the view factor solution is 28% off. The reason why both numerical models fail to predict the correct heat flux in the entire temperature range could lay in some unaccounted-for temperature dependency, such as change of Young's modulus.

Only steady-state–quantities were measured in the experiment. Tausendschön and Radl (Tausendschöen & Radl, 2021) report a physical time of 70 000 s as the typical time for the heat transfer simulations to reach the steady state. In our simulations, the steady state is reached much sooner: for example, at 400 °C, 90% of the final mean particle temperature is reached already at 3100 s. However, this discrepancy might be due to differences in

Table 7
Boundary conditions used for the SANA test case (Stöcker & Niessen, 1997).

Nominal power		**5 kW**	**35 kW**	z [cm]
outer boundary temperature	T_{C1}	326 K	449 K	0–6
	T_{C2}	334 K	499 K	6–15
	T_{C3}	358 K	574 K	15–85
	T_{C4}	374 K	595 K	85–94
	T_{C5}	367 K	569 K	94–100
protective tube temperature	T_{H1}	578 K	1498 K	0–15
	T_{H2}	650 K	1524 K	15–85
	T_{H3}	703 K	1523 K	85–100

Table 8
Simulation parameters used for the SANA test case (Stöcker & Niessen, 1997).

Parameter	Value
graphite heat capacity	closure from Entegris, 2013
particle-fluid convection	Li and Mason, 2000
fluid viscosity	Sutherland, 1893
fluid heat capacity	closure from ToolBox, 2004
drag model	Koch and Hill, 2001

definitions, as it is not clear what is understood by the "steady state" in (Tausendschöen & Radl, 2021).

Furthermore, the view-factor–based simulations are reported to typically take 671 s of computational time. Our model takes 335 s to simulate 70 000 s (keeping identical time step duration, initial temperature distribution, and particle heat capacity as in (Tausendschöen & Radl, 2021)). However, as the transient process ends sooner, the simulation could have been truncated already at 10 000 s of simulated time, taking only 50 s of computational time.

3.4.2. *Pebble bed with nitrogen: validation with data from the SANA test facility*

Next we replicate the pebble bed setup from the SANA test facility (Stöcker & Niessen, 1997). This experimental data is often used to validate codes intended for assessing nuclear safety (Baggemann et al., 2016; Niu & Wang, 2019; Novak et al., 2019).

The nuclear reactor used in the SANA experiments carries around 9500 pebbles. The height of the pebble bed is 1 m, and the diameter is 1.5 m. A heating element is placed in the centre of the bed. A protective graphite tube with 141 mm diameter separates

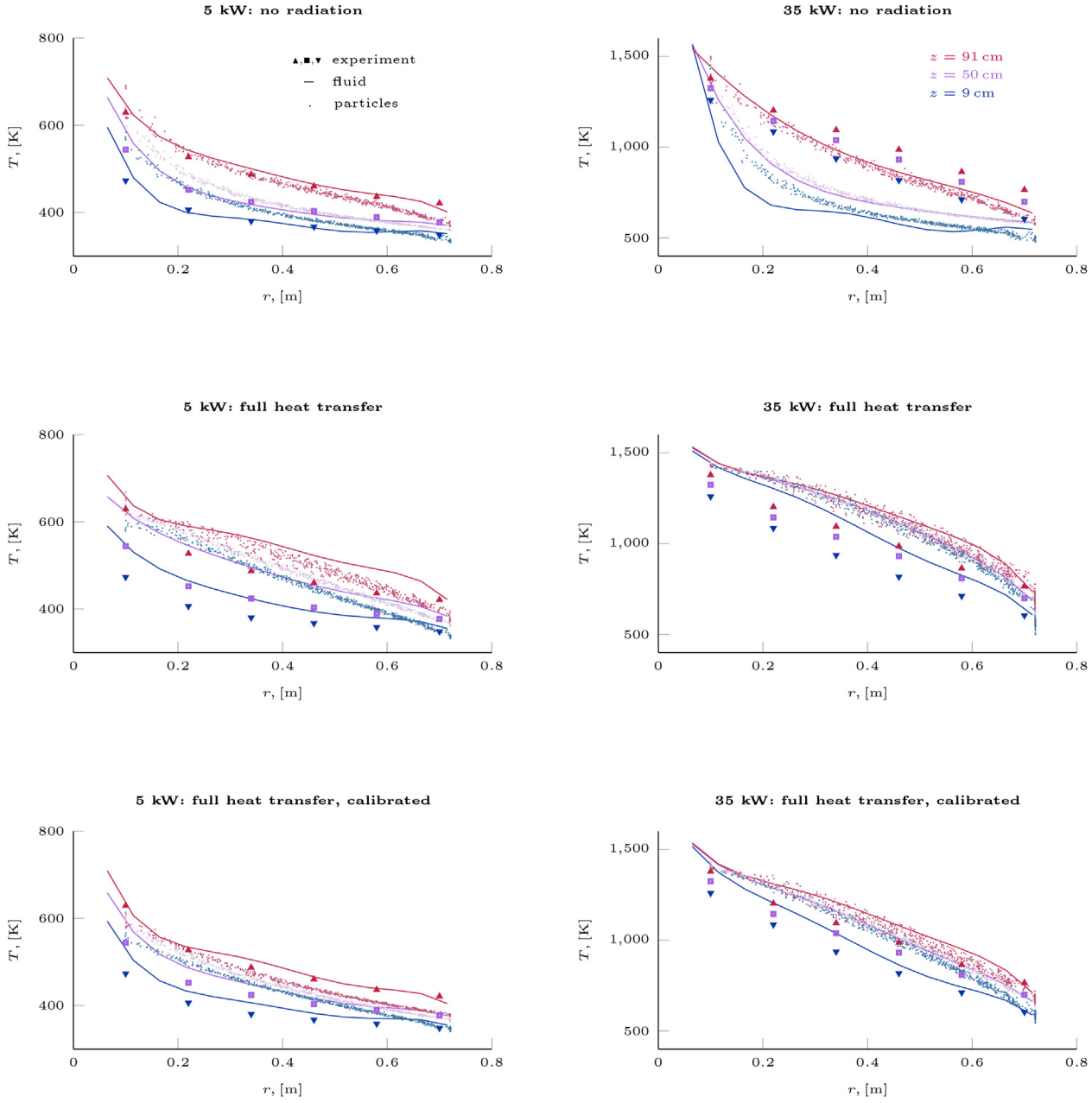

Fig. 17. Influence of simulation parameters on the temperature distribution across radial direction (fixed temperature boundary condition). Numerical results for fluid and particle temperature against experimentally measured particle temperature (Stöcker & Niessen, 1997).

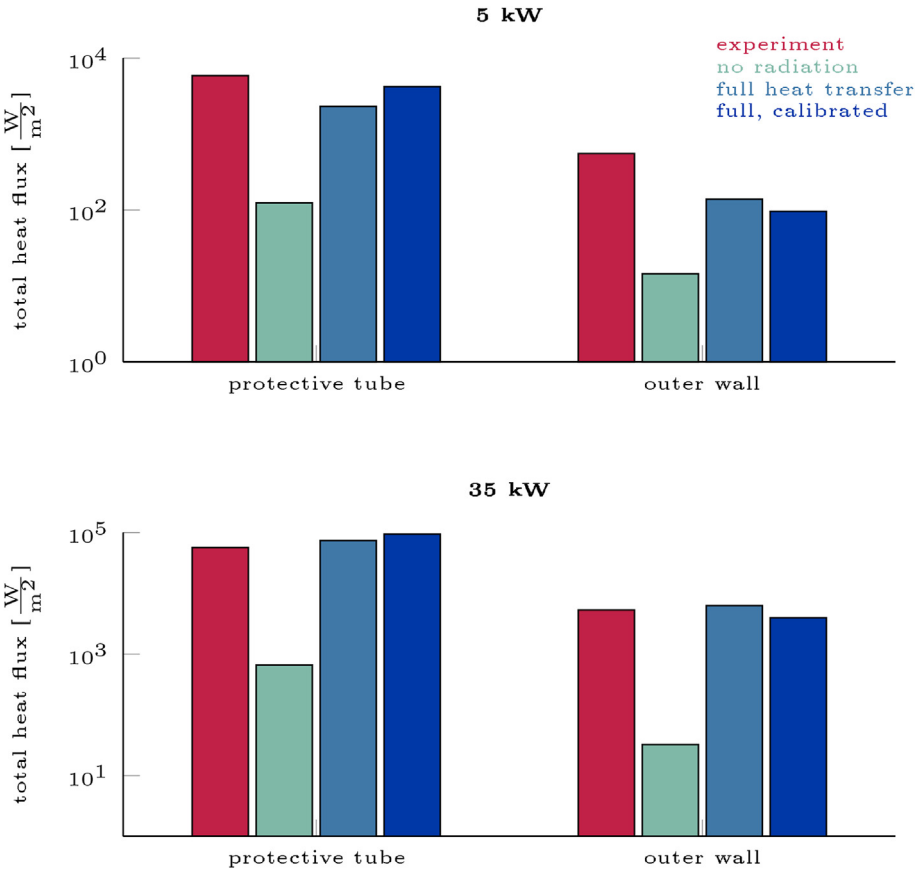

Fig. 18. Steady-state heat flux at domain boundaries (fixed temperature boundary condition).

the pebbles from the heating element. Pebbles are the same as described in the previous section, with 6 cm diameter.

The simulation domain is shown in Fig. 16. The protective graphite tube and the outer bed wall are split into sections, each with temperature assigned according to the experimental measurements (see Table 7). Top and bottom of the vessel are insulated and assumed to be non-participating in the simulation.

The pebble bed is filled with nitrogen at 1 bar. Presence of nitrogen gives rise to natural convection. To account for this, we use OpenFOAM's "buoyantPimpleFoam" as the basis for the fluid flow calculations (OpenFOAM, 2018). Solid-fluid interaction parameters are given in Table 8.

Since the pebbles are the same as used in the experiment with vacuum conditions (De Beer, 2014), conduction and radiation parameters are first kept as given in Table 5. However, as will be discussed later, this leads to an underestimation of the conductive contribution (see top and middle row in Fig. 17).

In contrast to vacuum conditions, the conductive transport does not happen only through the pebble-pebble contact area, but also through the thin layer of stagnant gas near the contact points. To take this effect into account, we increase the corrective Young's modulus from $Y_{orig} = 11.5$ GPa (Entegris, 2013) to $Y_{orig} = 11.5$ MPa, which yields approximatively 10 times larger contact area. Furthermore, the thermal conductivity of graphite decreases with temperature (De Beer, 2014; Entegris, 2013; Stöcker & Niessen, 1997). However, this decrease in conduction through the pebble-pebble contact areas is effectively counterbalanced by the increase in stagnant gas conductivity (Ren et al., 2017). Thus, we also impose a constant conduction coefficient of 150 $\frac{W}{mk}$ (i.e., the value for graphite at 100 °C (Stöcker & Niessen, 1997)).

The resulting temperature distribution is illustrated in Fig. 17, where the top and middle row respectively show simulation results without radiation, and simulation results for full heat transfer, both with conductive properties as under vacuum. The bottom row in Fig. 17 shows the full heat transfer, but with aforementioned calibration of conductive properties. The corresponding heat flux is illustrated in Fig. 18 (note the logarithmic scale). Since the heat flux is recorded only at the domain boundaries, no strategies for oscillation removal are used.

Judging from the temperature profile, the radiation contribution is miniscule in the low-power case, since the simulation without radiation yielded fluid temperatures that are nearly perfectly matching the experiment (Fig. 17, top left). On the other hand, the particle temperature is slightly overestimated near the reactor bottom. This suggests that the conductive transport is underestimated, even without radiative contribution. In the high-power case, temperatures are 20% lower than the experimental data (Fig. 17, top right). Also, the heat flux is severely underestimated: for both low- and high-power case, neglecting to include radiation resulted in a heat flux several magnitudes lower than that imposed in the experiment (Fig. 18).

Inclusion of radiation yields a heat flux closer to the experimental values, but also leads to the overestimation of temperatures (Fig. 17, middle left and right).

Finally, adding also the conduction contribution due to the gas near the contact points reduces the mean fluid temperature error in both cases to less than 10% (Fig. 17, bottom left and right). However, the temperatures in the high-power case are still exaggerated. Also, while the fluid temperature displays a buoyancy-induced vertical distribution as recorded in the experiment, the particle

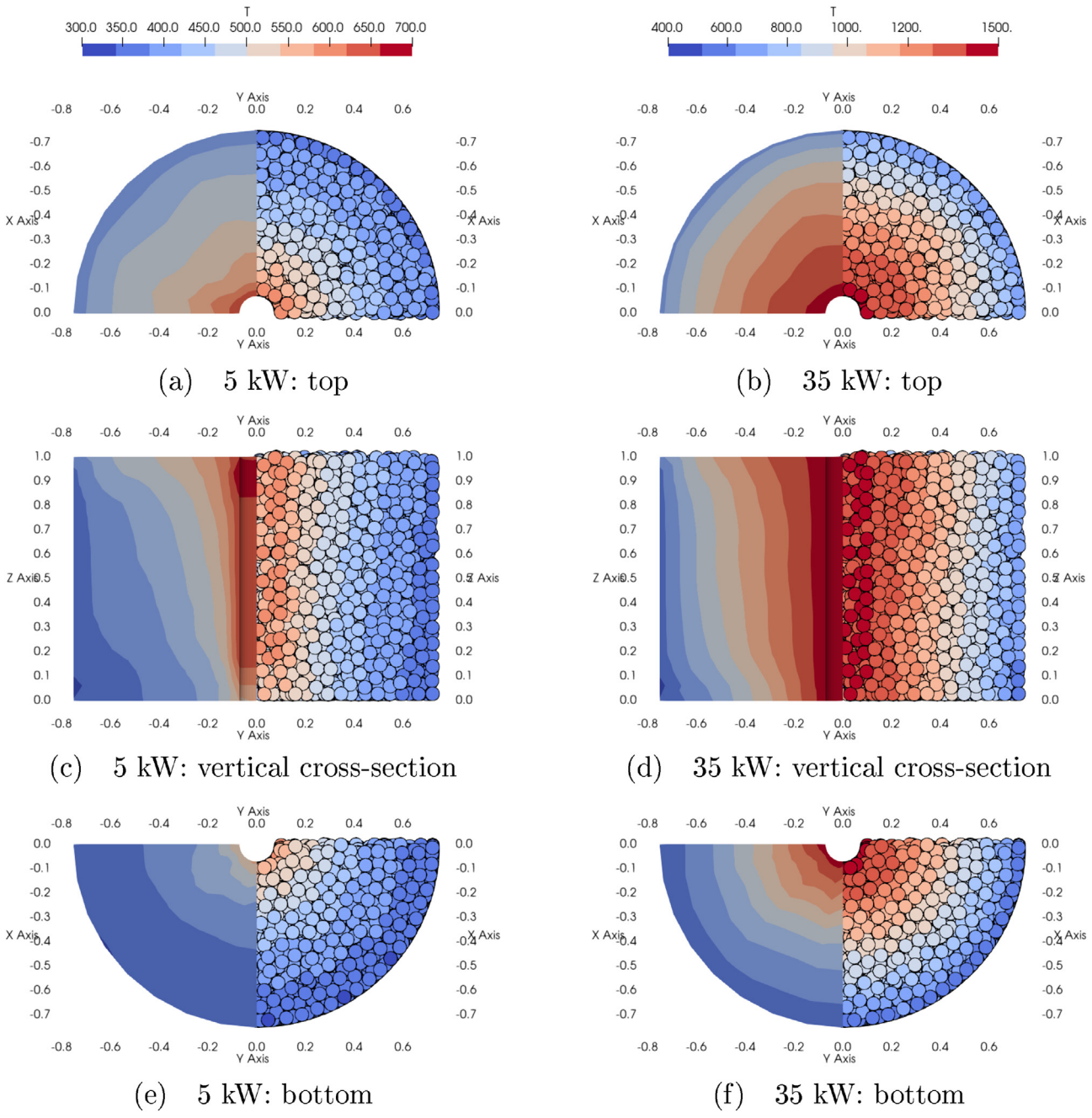

Fig. 19. Temperature distribution (fixed temperature boundary condition).

temperature profile is more uniform. This is especially pronounced in the high-temperature case.

The experimental heat flux displayed in Fig. 18 is calculated from the effective power divided by the surface area of the boundary. After subtracting losses from the electrodes and water cooling (Stöcker & Niessen, 1997), the nominal powers of 5 kW and 35 kW amount to effective powers of respectively 2.6 kW and 25.16 kW. Final simulation results (calibrated full heat transfer) yielded error of 30% and 70% at the protective tube, and of 117% and 170% at the outer boundary, respectively for the low- and the high-power case.

Snapshot of the temperature distribution for the calibrated simulation is shown in Fig. 19. The left-hand side of each view represents fluid values, and right-hand side particle values.

Additionally, we show the temperature distribution for the situation where a constant radiative heat flux is imposed at the protective tube boundary. The heat flux measured in experiments is not purely radiative: the heating element radiatively heats up the graphite protective tube, which in turn heats up the pebbles and the nitrogen via all three modes of heat transfer. Still, as a complex multiphase heat flux boundary condition is out of the scope of our current work, we treat the heat flux as purely radiative, and impose a zero-gradient temperature condition for the fluid. The outer wall boundary remains as described previously.

As seen from Fig. 20, in the case of an imposed heat flux, the influence of conductivity seems to be overestimated. Here, the low-power case barely heats-up. The high-power case also results in

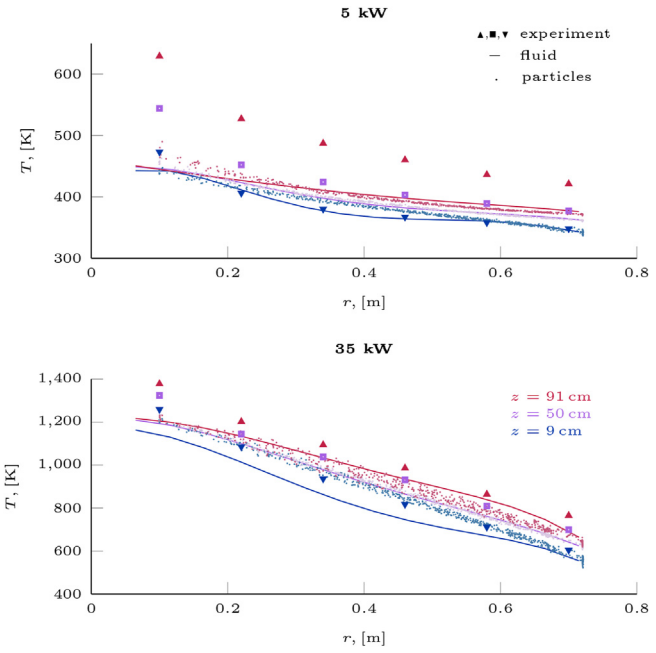

Fig. 20. Temperature distribution in the radial direction (fixed radiative heat flux boundary condition). Numerical results for fluid and particle temperature against experimentally measured particle temperature (Stöcker & Niessen, 1997).

overall lower temperatures. Snapshots of the temperature distribution are given in Fig. 21.

The sources of discrepancy between our results and the experimental data could be attributed to imprecise boundary conditions and to the scale of the particles. First, the walls in simulation are treated as infinitely thin. However, the temperatures from Table 7 are measured at a certain distance from the pebble bed. Detailed simulations (Baggemann et al., 2016) show that the temperature field significantly decays through the protective tube, which explains the large departure in the high-power case. Second, pebbles in our simulation are assumed to have constant temperature. Being quite large (6 cm in diameter) it is reasonable to assume that a temperature gradient over each pebble exists.

More successful attempts at recreating this experiment can be found in literature. For example, Baggeman et al. (Baggemann et al., 2016) presented an almost perfect agreement using a porous media approach. The pebble bed geometry was described in detail, including the electrodes, heating element, and the protective tube. Radiation was taken into account via an effective conductivity of the solid phase. The axial symmetry of the case was used to reduce the problem into two dimensions, resulting in a grid of 55 000 elements. Novak et al. (Novak et al., 2019) also used a porous media approach, with radiation handled implicitly with an effective conductivity. The mean temperature error was reported to be within 25 °C (grid data unknown). Niu and Wang (Niu & Wang, 2019), used a resolved CFD-DEM approach. The contact points between the pebbles were modelled using cylindrical bridges of radius $r_c = 0.1d_p$. An unstructured grid with five layers of prismatic mesh elements was applied at the fluid-solid interfaces. To reduce the computational effort, only one quarter of the bed was simulated, numbering 37 million computational elements. Radiation was modelled using a surface-to-surface (view factor) approach.

While our simplified approach cannot compete in precision with detailed simulations, we were able to successfully predict general trends using extremely low computational effort. Unfortunately, computational times were not reported in literature, so a direct comparison is not possible. However, with 9428 Lagrangian computational points and 4096 Eulerian cells, we represented the entire geometry of the bed. Baggeman et al. (Baggemann et al., 2016) used 4 times as much cells to represent a single slice of the domain, while Niu and Wang (Niu & Wang, 2019) used approximately 2000 times more cells to represent a quarter of the domain. Our slowest-running case (5 kW, fixed temperature boundary condition), split on two processors, took only 1770 s of computational time.

4. Conclusion

This work explored radiation modeling via the P1 approximation in the context of combined computational fluid dynamics and discrete element method (CFD-DEM).

Due to its simple mathematical formulation, the P1 approximation is a popular radiation model, often used in multiphysics industrial-scale simulations. However, being approximative, the P1 model performs well only in the case of optically thick, and homogeneous media.

Granular media is often optically thick: we show that in dilute packings, with a solid fraction of 0.1, a length of only 60 particle diameters is needed to effectively constitute an opaque medium. In dense packings, with a solid fraction of 0.5, this number reduces to 6 particle diameters.

The homogeneity constraint is more challenging. Randomly distributed particles create spatial variations of solid fraction and therefore also variations of radiative properties. Any sharp, discretization-induced fluctuation is mathematically analogous to an existence of immiscible fluids with an interface, where the radiative transport equation predicts temperature jumps. We demonstrate this by developing an approximate solution for a one-dimensional bed with a step change in solid fraction. While the P1 model fails to predict the temperature jump, the abrupt change of opacity gives rise to heat flux oscillations.

Dilute and dense regions of a particle bed have no sharp interface, hence no temperature jump should be discernible. The tendency of the P1 model to settle at some medium interfacial temperature therefore produces the anticipated results. However, the oscillations in heat flux can cause severe errors if the computational grid is relatively small compared to the particle size, leading to intermittent occurrence of densely packed cells, and cells completely devoid of particles.

In that case, the mean heat flux (averaged over the domain) can be remedied by employing smoothing of the radiative diffusion, or by pseudo-scattering. Smoothing is a standard procedure, often used to improve the temporal behaviour of the solid fraction and the particle-fluid momentum exchange terms, while pseudo-scattering artificially increases the scattering contribution of the fluid. Both procedures assuage the heat flux oscillations by reducing the disparity of attenuation properties between the adjacent particle-filled and particle-empty cells.

Smoothing outperforms pseudo-scattering almost always; pseudo-scattering is useful for relatively small domains, with less than 1000 particles.

Both smoothing and pseudo-scattering remove the extreme heat flux oscillations, improving the prediction of the mean heat flux. However, dispersion of local heat flux values persists even after an oscillation-removal strategy is employed. Therefore, the P1 model appears less suitable for studying changes of heat flux across the domain.

Still, excellent agreement with an analytical solution is obtained for the steady-state temperature distribution, and for the mean steady-state heat flux. The model also reliably predicts the transient behaviour: cooling and heating of a single particle agrees with

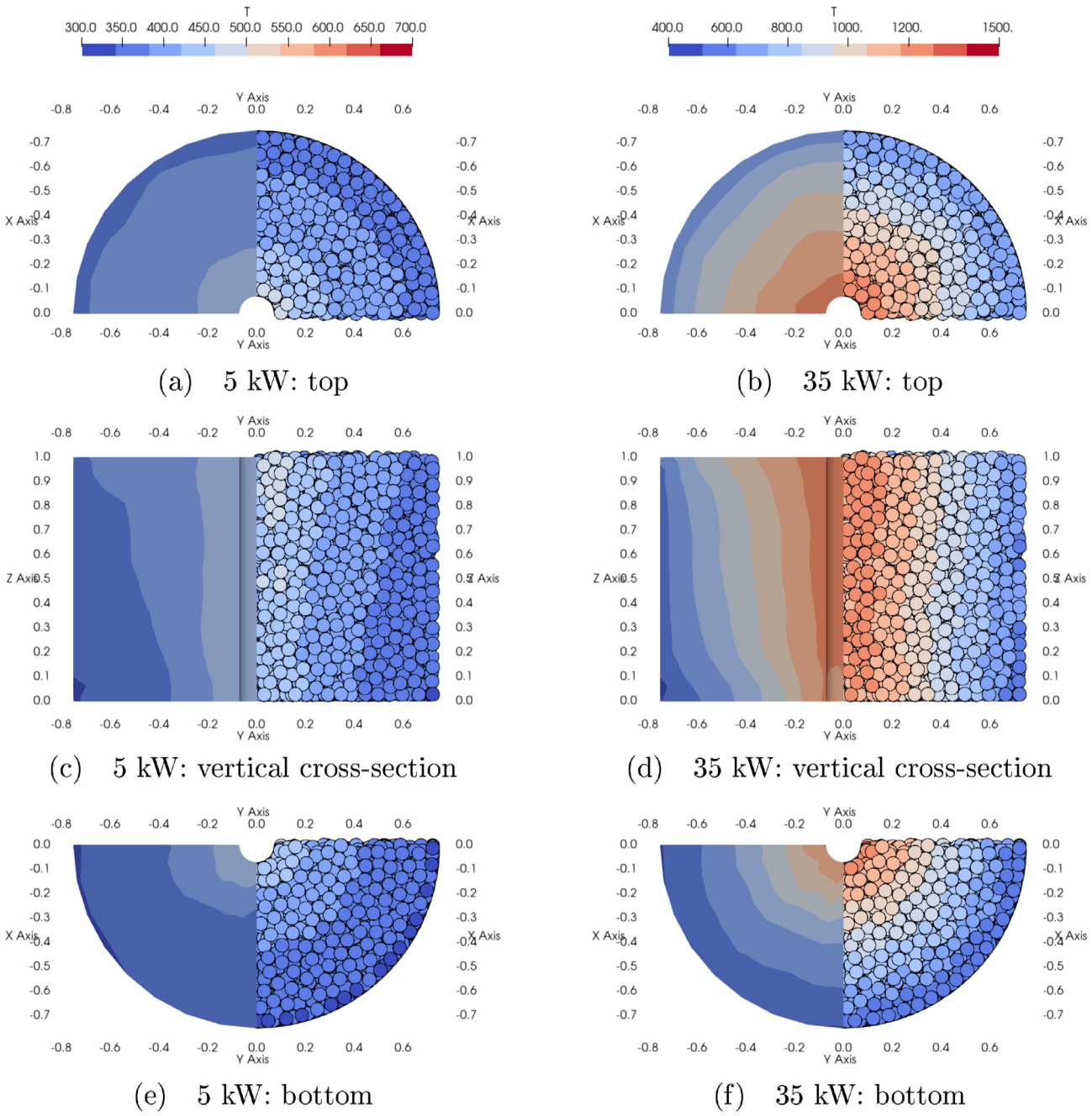

Fig. 21. Temperature distribution (fixed radiative heat flux boundary condition).

an analytical solution, and cooling of a particle mixture agrees with a semi-analytical solution.

Precision is retained for size-disperse systems, with various absorption characteristics.

Dependent scattering effects are taken into account using Brewster's closure (Brewster, 2004). While dependent scattering is often overlooked (Li & Chandran, 2022), we found that neglecting this term leads to an inaccurate mean heat flux (i.e., an increase of $\approx$60%) and also affects the transients.

With an appropriate closure, the applicability to coarse-graining is practically limitless: we found no discernible difference in the results by varying coarse-graining level to up to a million.

In comparison with experimental data, satisfactory agreement is found for an application in vacuum. The steady-state temperature and the (mean) heat flux are of similar precision as predictions of a view-factor–based approach. In the presence of an interstitial fluid, calibration is necessary to represent the conduction correctly (i.e., to account for surface roughness, and fluid at contact points). With calibration, it is possible to obtain a temperature distribution within 10% margin of error. The predictions could have been potentially improved by more accurate boundary conditions, and by introducing an intra-particle temperature distribution.

While the more precise radiation models take up most of the computational time, the P1 approximation is extremely fast, and, alongside proper calibration of other heat transfer properties, has the potential to also be very accurate. Used on its own, the P1 model has the capacity to reliably predict trends, and in conjunction with a

$$t_2 - t_1 = \left(\frac{\rho_p c_p d_p}{24 Q_{abs} \sigma T_0^3} \left(2\arctan\left(\frac{T_p}{T_0}\right) - \ln\left(\frac{|T_p - T_0|}{T_p + T_0}\right) \right) \right) \Bigg|_{T_{p,1}}^{T_{p,2}} = C_\tau \left[2\left(\arctan\left(\frac{T_{p,2}}{T_0}\right) - \arctan\left(\frac{T_{p,1}}{T_0}\right) \right) + \ln\left(\frac{|T_{p,1} - T_0|}{T_{p,1} + T_0} \cdot \frac{T_{p,2} + T_0}{|T_{p,2} - T_0|} \right) \right], \tag{36}$$

more elaborate method, it can immensely speed up the simulation process.

Declaration of competing interest

The authors declare that they have no known competing financial interests or personal relationships that could have appeared to influence the work reported in this paper.

Acknowledgements

This project is funded through Marie SKŁODOWSKA-CURIE Innovative Training Network **MATHEGRAM**, the People Programme (Marie SKŁODOWSKA-CURIE Actions) of the European Union's Horizon 2020 Programme H2020 under REA grant agreement No.813202.

Appendices

A. Transient heat transfer

To verify the transient behaviour of the P1 model, we study temperature evolution of: a) a solitary particle in an isothermal black enclosure, and b) a packed bed placed between two isothermal black plates. For the first case, we find an analytical solution alongside important dimensionless parameters, and for the second case, we use the semi-analytical solution for a continuous gray medium given by Lipiński and Steinfeld (Lipiński & Steinfeld, 2005).

A.1. Solitary particle in an isothermal enclosure

We study temperature evolution of a single black particle placed in an isothermal black enclosure (Fig. A1).

The particle is fully enveloped by the enclosure, therefore all emitted and absorbed power is spent into the change of the particle's internal energy:

$$\rho_p c_p \frac{\pi d_p^3}{6} \frac{\mathrm{d}T_p}{\mathrm{d}t} = Q_{abs} \frac{\pi d_p^2}{4} \left(4\sigma T_0^4 - 4\sigma T_p^4 \right). \tag{34}$$

Meaning of the symbols in the equation above is summarized in Table A1.

A similar test case was used in (Amberger et al., 2013), where Monte Carlo simulation was compared to direct forward Euler time integration of Stefan-Boltzmann's law. Since Eq. (34) is an ordinary differential equation, we re-write it to:

$$\mathrm{d}t = \frac{\rho_p c_p d_p}{6 Q_{abs} \sigma} \frac{\mathrm{d}T_p}{T_0^4 - T_p^4}. \tag{35}$$

Integrating the above from state 1 ($t = t_1$, $T_p = T_{p,1}$) to state 2 ($t = t_2$, $T_p = T_{p,2}$) results in:

where

$$C_\tau = \frac{\rho_p c_p d_p}{24 Q_{abs} \sigma T_0^3} \tag{37}$$

is extracted as the characteristic time constant of the system.

Next we compare the simulation results to Eq. (36). Two situations are considered: particle cooling ($T_{p,1} > T_0$) and particle heating ($T_{p,1} < T_0$). Simulation parameters are defined in Table A1. The effect of the enclosure temperature T_0 on the time constant should be emphasized: as seen in this example, using 2 times larger enclosure temperature results in 8 times smaller time constant, due to inverse proportionality to the third-power.

The time evolution of the particle temperature is given in dimensionless form in Fig. A2. Using the 20-th part of the time constant C_τ as the time step yields relative mean error of 3.9% for cooling and 3.7% for heating. The largest discrepancies are at the start of the simulation. By decreasing the time step, it is possible to further improve precision: e.g. time step of $C_\tau/100$ in the cooling simulation reduced the mean error to 0.9%.

Changing the length of the enclosure side from 1 m to 10 m did not affect the simulation results, which is not surprising since the enclosure size does not enter Eq. (34). The test case is also insensitive to the mesh resolution, as the discrepancies in the results stayed below 1% for meshes of 3, 5, 9, and 15 cells per enclosure side length.

A.2. Cooling of a packed bed

Lipiński and Steinfeld (Lipiński & Steinfeld, 2005) developed a semi-analytical solution to verify the Monte Carlo method for transient radiative heat transfer in suspensions of coal particles. We adapt here the same solution to evaluate the P1 model in granular media.

The semi-analytical solution is derived for a continuous gray medium between two isothermal black plates at a temperature T_w. The temperature profile established in the medium is given in the dimensionless time instances:

$$\tilde{t} = \frac{4\sigma T_{p,0}^3}{\varphi_p \rho_p c_p L} t, \tag{38}$$

where $T_{p,0}$ is the initial particle temperature, φ_p the solid fraction, ρ_p the particle density, c_p the particle heat capacity, L the length of the domain, and σ the Stefan-Boltzmann constant.

We test three simulation setups as shown in Fig. A3: a) a uniformly packed monodispersion, b) a randomly packed monodispersion, and c) a randomly packed polydispersion.

Particle initial temperature is set to $T_{p,0} = 1000$ K, and wall boundaries are set to $T_w = 300$ K. The rest of the simulation parameters is given in Table 2. Particle properties are as defined for the monodisperse and polydisperse case in Table 3. To recreate the

setup from (Lipiński & Steinfeld, 2005), the absorption to scattering ratio is fixed at 0.535, with an overall opacity of $\tau_L = 2$.

Fig. A4 shows the simulation results against the semi-analytical solution (Lipiński & Steinfeld, 2005). For the uniform monodisperse packing, the mean difference stays below 2%, while it rises to about 5% for the other two cases. The maximum difference of 12% is found for the polydisperse packing, due to different heatings rates for different-sized particles.

Tested for the polydispersion, decreasing the time step (from 1 s to 0.1 s), varying the mesh resolution (from 10 to 100 cells per length), as well as adding the correction procedures (i.e., smoothing with $L_{smooth} = 2d_p$ and pseudo-scattering with $\varsigma_f = 10\%\beta$), did not alter the results for more than 1%.

Recently, Díaz-Heras et al. (Díaz-Heras et al., 2021) applied the P1 model to study an irradiated bubbling fluidized bed. A departure from experimental data was observed regarding the time evolution of the mean particle temperature. As our results verify that the P1 model is able to accurately predict transient heat-up in a radiation-only situation, the error reported in (Díaz-Heras et al., 2021) could be attributed to some other factor present in experimental conditions. Still, future research might be needed to increase the fidelity of the simulation model.

B. Influence of particle size and absorption properties

It is established in subsection 3.2, that the steady-state is nearly identical for size-disperse systems of the same opacity. Moreover, since the opacity is determined by the overall extinction, the relative amount of absorption and scattering contributions is also inconsequential. The only exception where the ratio of absorption and scattering affects the steady-state is the limiting case of pure scattering: here, no energy is absorbed and the medium remains isothermal.

However, particle size and absorption coefficient do affect the transients. To demonstrate this effect, we use the setup from subsection 3.2.1 at opacity $\tau_L = 10$. We consider the moment when the average particle reaches 90% of its steady-state value as the equilibrium ($\Delta t_{90\%}$), i.e., the end of the transient heat-up phase.

In the case of pure absorption ($Q_{abs}/Q_{ext} = 1$), the equilibrium times of 1020 s, 403 s, and 870 s are found respectively for the monodispersion, bidispersion, and polydispersion. Remembering Eq. (37), the characteristic time is proportional to the particle diameter and the material density. The equilibrium times thus correlate to the total mass of the system: as defined in Table 3, the monodispersion has the highest mass and accordingly takes the longest time to settle. On the other side, the bidispersion features the smallest particles and thus the fastest change.

Furthermore, reducing the absorption contribution, while keeping the extinction constant, will increase the duration of the transient phase. As seen in Fig. B1, case with 10% absorption and 90% scattering caused a prolongation of ≈15% for the bidispersion, and of ≈25% for the monodispersion and the polydispersion.

Meanwhile, there is virtually no difference between the steady-state values for various Q_{abs}/Q_{ext} ratios. Captured at 5000 s, the discrepancy is below 0.2% for temperature, and below 0.04% for the heat flux. The same heat flux is found also for pure scattering, while the particle temperature remained at its initial value.

C. Imposed radiative heat flux at boundaries

Many applications, such as solar or laser heating, need to impose a radiative heat flux at the boundaries. Here, this is possible according to Eq. (14). For verification, we use an analogous test case to the one from subsection 3.2. We keep the temperature fixed at the cold boundary, but impose a constant heat flux from Eq. (27) at the opposite side.

The resulting temperatures at the boundary with the fixed heat flux applied are shown in relation to the number of cells per length in Fig. C1. Displayed results are for the polydisperion from Table 3 at opacity $\tau_L = 10$.

While the error in regard to Eq. (25) remains below 5%, both smoothing and pseudo-scattering introduce unboundedness of the temperature. Heat flux corrections of intermediate magnitude cause the overshoot of the theoretically possible temperature slip, while high-magnitude corrections lead to the overshoot of the theoretical wall temperature.

Since the spatial distribution of particles is the same as in subsection 3.2.3, local heat flux values are dispersed with an identical coefficient of variation, while the overall mean heat flux achieves the same or slightly better precision.

D. Gray walls

For simplicity, we assumed black enclosure walls in all previous verification cases. Since gray walls are more common in practice, we also briefly show results for such a situation.

The test case setup is as described in subsection 3.2.1, with wall emissivities reduced to 0.8 and 0.2. We consider the polydisperse case from Table 3 at $\tau_L = 10$.

The resulting steady-state emissive power is shown against the analytical solution from (Heaslet & Warming, 1965) in Fig. D1. Compared to Eq. (25), the temperature discrepancy stayed below 2%: the maximum error amounts to 0.26% when the higher emissivity is at the hot wall ($\varepsilon_{w1} = 0.8$), and to 1.38% in the opposite case ($\varepsilon_{w2} = 0.8$). The error in the mean heat flux is in the former and latter case respectively 9.76% and 7.86% according to Eq. (28).

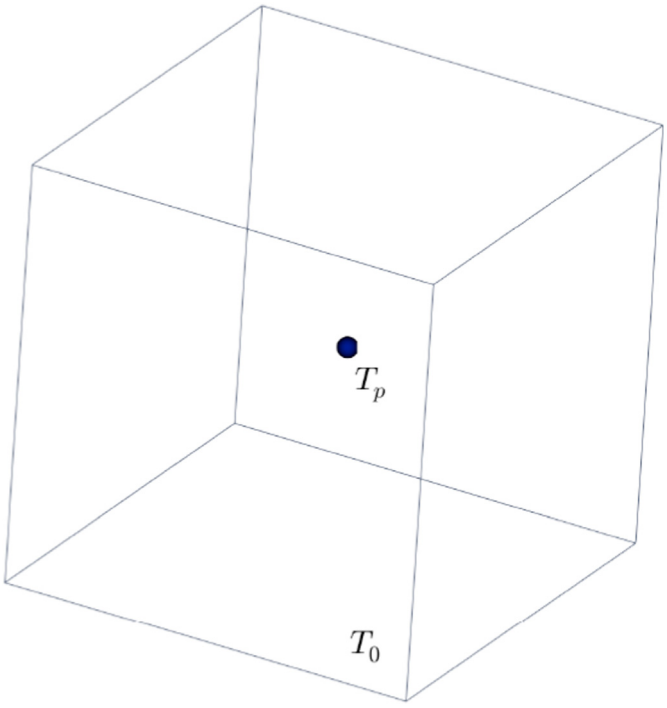

Fig. A1. Solitary particle in an isothermal enclosure.

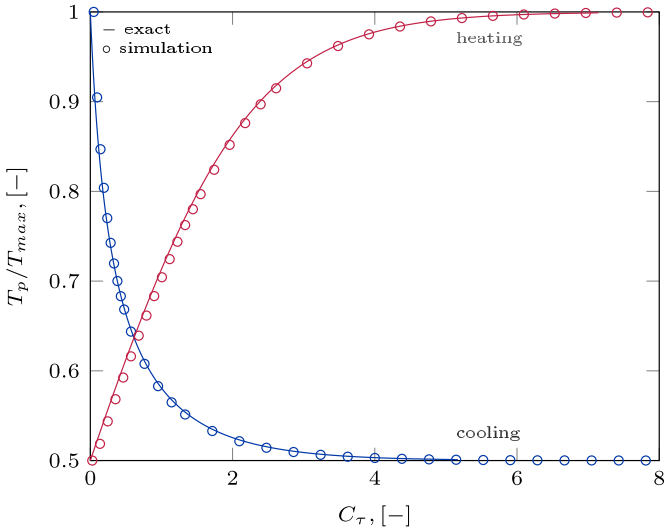

Fig. A2. Temperature of a solitary black particle in an isothermal black enclosure.

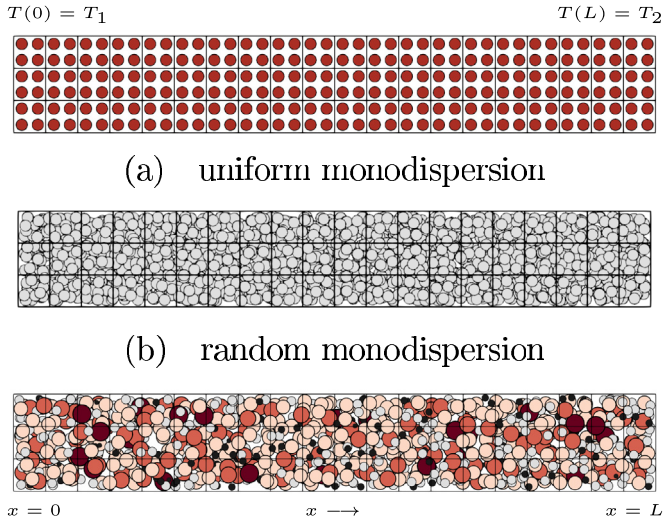

Fig. A3. Simulation domain for transient simulations.

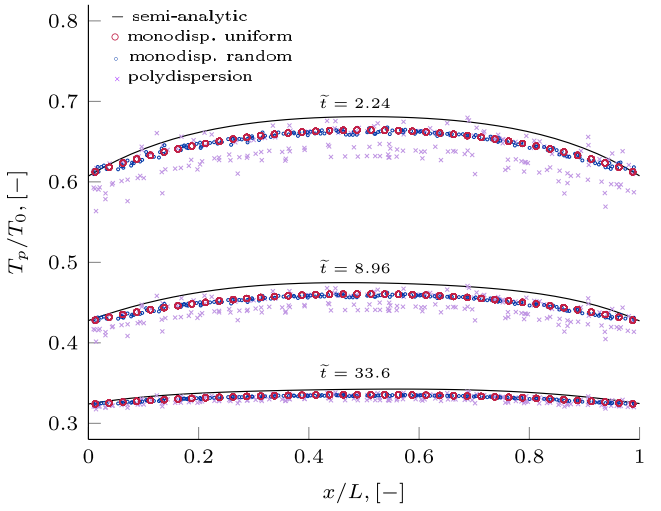

Fig. A4. Temperature profiles for a medium with $\tau_L = 2$. Setup from Table 2 compared to the semi-analytic solution from (Lipiński & Steinfeld, 2005).

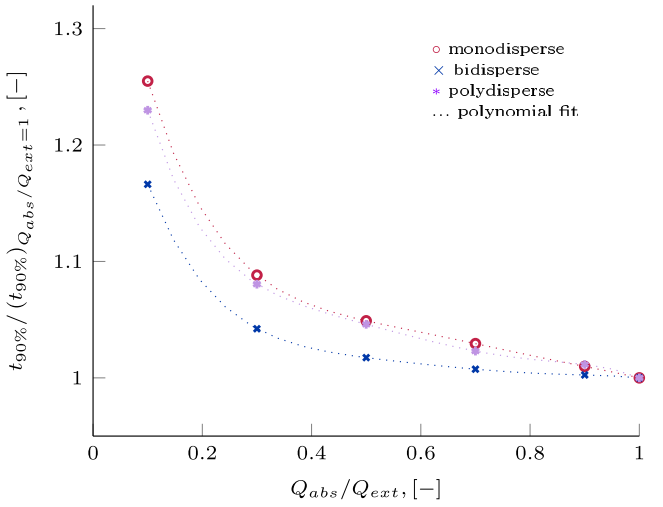

Fig. B1. Effect of absorption to extinction efficiency ratio on the time needed to reach the equilibrium in a medium with $\tau = 10$ (setup from Table 2).

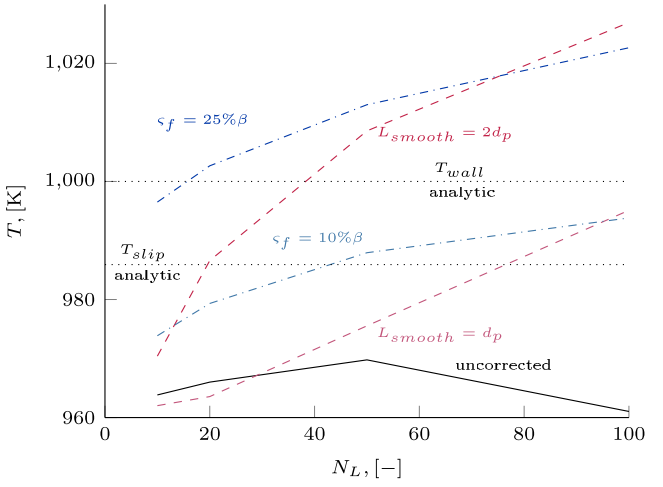

Fig. C1. Temperature established next to the hot wall under a prescribed heat flux versus number of cells per length N_L (polydispersion with opacity $\tau_L = 10$ from Table 3).

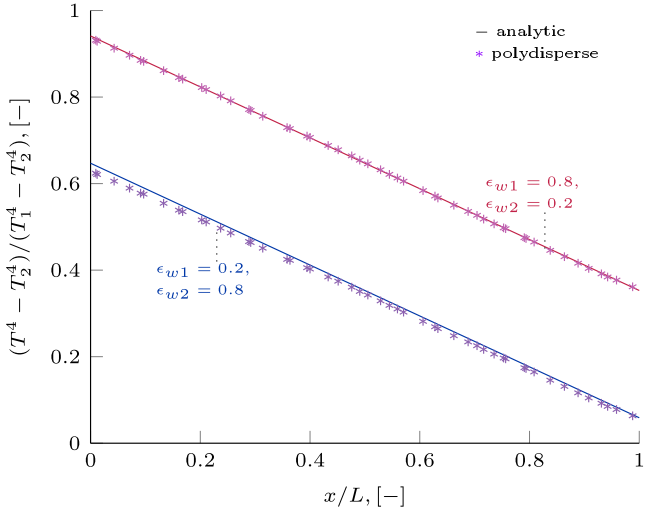

Fig. D1. Emissive power established in a polydispersion with opacity $\tau_L = 10$ placed between gray walls (setup from Table 3).

Table A1
Solitary particle in an isothermal enclosure—simulation parameters.

Parameter	Value
density	$\rho_p = 1000\ \frac{\text{kg}}{\text{m}^3}$
heat capacity	$c_p = 1000\ \frac{\text{J}}{\text{kgK}}$
particle diameter	$d_p = 0.05$ m
absorption efficiency	$Q_{abs} = 1$
enclosure wall emissivity	$\epsilon_w = 1$
enclosure side length	1 m, 10 m
mesh resolution per enclosure side	3, 5, 9, 15
simulation duration	$8C_\tau$
time step	$C_\tau/20$
Cooling	
initial particle temperature	$T_{p,1} = 1000$ K
enclosure temperature	$T_0 = 500$ K
time constant	$C_\tau \approx 300$ s
Heating	
initial particle temperature	$T_{p,1} = 500$ K
enclosure temperature	$T_0 = 1000$ K
time constant	$C_\tau \approx 40$ s

References

Amberger, S., Pirker, S., & Kloss, C. (2013). Thermal radiation modeling using ray tracing in LIGGGHTS. *Proceedings of DEM, 6*.

Baggemann, J., Shi, D., Kasselmann, S., Kelm, S., Allelein, H.-J., & Hurtado, A. (2016). Use of SANA experimental data for validation and verification of MGT-3D and CFD porous media model for VHRT application. *Nuclear Engineering and Design, 305*, 678–687.

Bellan, S., Gokon, N., Matsubara, K., Cheok, C. H., & Kodama, T. (2018). Heat transfer analysis of 5kW$_{th}$ circulating fluidized bed reactor for solar gasification using concentrated Xe light radiation. *Energy, 160*, 245–256.

Brewster, Q. (2004). Volume scattering of radiation in packed beds of large, opaque spheres. *Journal of Heat Transfer, 126*, 1048–1050.

Capecelatro, J., & Desjardins, O. (2013). An Euler-Lagrange strategy for simulating particle-laden flows. *Journal of Computational Physics, 238*, 1–31.

CFDEMcoupling open source CFD-DEM framework. https://www.cfdem.com/cfdemrcoupling-open-source-cfd-dem-framework, (2011)–. (Accessed 4 November 2022).

CFDEMcoupling documentation: Divided void fraction command. https://www.cfdem.com/media/CFDEM/docu/voidFractionModel_dividedVoidFraction.html, (2016)–. (Accessed 11 May 2022).

CFDEMcoupling documentation: "constdiffsmoothing" command. https://www.cfdem.com/media/CFDEM/docu/smoothingModel_constDiffSmoothing.html, (2016)–. (Accessed 11 May 2022).

Chandrasekhar, S. (1950). *Radiative transfer*. Oxford University Press.

Chen, J., Kumar, A., Coventry, J., Kim, J., & Lipiński, W. (2022). Numerical modelling of radiative heat transfer in a polydispersion of ceramic particles under direct high-flux solar irradiation. *Journal of Quantitative Spectroscopy & Radiative Transfer, 278*, Article 108008.

Cintolesi, C., Nilsson, H., Petronio, A., & Armenio, V. (2017). Numerical simulation of conjugate heat transfer and surface radiative heat transfer using the p1 thermal radiation model: Parametric study in benchmark cases. *International Journal of Heat and Mass Transfer, 107*, 956–971.

De Beer, M. (2014). *Characterisation of thermal radiation in the near-wall region of a packed pebble bed, Master's thesis*. North-West University.

Díaz-Heras, M., Córcoles, J. I., Belmonte, J. F., & Almendros-Ibáñez, J. A. (2021). 3D numerical simulation of a directly irradiated bubbling fluidized bed with SiC particles. *Applied Thermal Engineering, 190*, Article 116812.

Dombrovsky, L. A. (1997). Evaluation of the error of the P1 approximation in calculations of thermal radiation transfer in optically inhomogeneous media. *High Temperature, 35*, 676–679.

Dombrovsky, L. A. (2010). Estimate of P1 error for optically inhomogeneous media. https://thermopedia.com/content/134/. (Accessed 25 March 2021).

Entegris. (2013). *Properties and characteristics of graphite for the semiconductor industry*. https://www.entegris.com/.

Forgber, T., & Radl, S. (2018). A novel approach to calculate radiative thermal exchange in coupled particle simulatons. *Powder Technology, 323*, 24–44.

Goniva, C., Kloss, C., Deen, N., Kuipers, J. A. M., & Priker, S. (2012). Influence of rolling friction modelling on single spout fluidized bed simulations. *Particuology, 10*, 582–591.

Greenshields, C. J. (2018). *OpenFOAM user Guide*. The OpenFOAM Foundation.

Gusarov, A. V. (2009). A model of averaged radiation transfer in two-phase heterogeneous medium. *High Temperature, 47*, 375–389.

Heaslet, M. A., & Warming, R. F. (1965). Radiative transport and wall temperature slip in an absorbing planar medium. *International Journal of Heat and Mass Transfer, 8*, 979–994.

Howell, J. R., Siegel, R., & Mengüç, M. P. (2010). *Thermal radiation heat transfer* (5th ed.). CRC Press.

Jeans, J. (1917). The equations of radiative transfer of energy. *Monthly Notices of the Royal Astronomical Society, 78*, 28–36.

Kloss, C., Goniva, C., Hager, A., Amberger, S., & Priker, S. (2012). Models, algorithms and validation for opensource DEM and CFD-DEM. *Progress in Computational Fluid Dynamics, 12*, 140–152.

Koch, D. L., & Hill, R. J. (2001). Inertial effects in suspension and porous-media flows. *Annual Review of Fluid Mechanics, 33*, 619–647.

Kong, D., Luo, K., Wang, S., Yu, J., & Fan, J. (2022). Particle behaviours of biomass gasification in a bubbling fluidized bed. *Chemical Engineering Journal, 428*, Article 131847.

Kopping, S. J., Hoeniges, J., Greenhagen, J., Matejczyk, Z., & Venstrom, L. J. (2019). Model of the solar-driven reduction of cobalt oxide in a particle suspension reactor. *Solar Energy, 177*, 713–723.

Ku, X., Li, T., & Løvås, T. (2015). CFD–DEM simulation of biomass gasification with steam in a fluidized bed reactor. *Chemical Engineering Science, 122*, 270–283.

Li, B., & Chandran, R. B. (2022). Effects of spatial correlations in particulate media on dependent scattering and radiative transport. *International Journal of Heat and Mass Transfer, 182*, Article 121951.

LIGGGHTS open source DEM particle simulation code. https://www.cfdem.com/liggghts-open-source-discrete-element-method -particle-simulation-code, (2011)–. (Accessed 4 November 2022).

Li, J., & Mason, D. J. (2000). A computational investigation of transient heat transfer in pneumatic transport of granular particles. *Powder Technology, 112*, 273–282.

Lipiński, W., & Steinfeld, A. (2005). Transient radiative heat transfer within suspension of coal particles undergoing steam gasification. *Heat and Mass Transfer, 41*, 1021–1032.

Liu, H., Elkamel, A., Lohi, A., & Biglari, M. (2013). Computational fluid dynamics modeling of biomass gasification in circulating fluidized-bed reactor using the Eulerian-Eulerian approach. *Industrial & Engineering Chemistry Research, 52*, 18162–18174.

Liu, B., Zhao, J., & Liu, L. (2021). Applicability of beer's law in particulate system from random to regular arrangement: A numerical evaluation. *Journal of Quantitative Spectroscopy & Radiative Transfer, 276*, Article 107938.

Mačak, J., Goniva, C., & Radl, S. (2021). Regimes of subsonic compressible flow in gas-particle systems. *Powder Technology, 394*, 44–61.

Marshak, R. (1947). Theory of the slowing down of neutrons by elastic collision with atomic nuclei. *Reviews of Modern Physics, 19*(3), 185–238.

Modest, M. F. (2013). *Radiative heat transfer* (3rd ed.). Elsevier.

Moukalled, F., Mangani, L., & Darwish, M. (2016). *The finite volume method in computational fluid dynamics: An advanced introduction with OpenFOAM® and Matlab®*. Springer.

Moumin, G., Tescari, S., Sundarraj, P., de Oliviera, L., Roeb, M., & Sattler, C. (2019). Solar treatment of cohesive particles in a directly irradiated rotary kiln. *Solar Energy, 182*, 480–490.

Niu, Q., & Wang, N.-X. (2019). Study of heat transfer by using dem–cfd method in a randomly packed pebble-bed reactor. *Nuclear Science and Techniques, 30*, 28.

Norouzi, H. R., Zarghami, R., S-G, R., & Mostoufi, N. (2016). *Coupled CFD-DEM modeling: Formulation, implementation and application to multiphase flows*. Wiley.

Novak, A. J., Peterson, J. W., Zou, L., Andrš, D., Slaybaugh, R. N., & Martineau. (2019). Validation of Pronghorn friction-dominated porous media thermal-hydraulics model with the SANA experiments. *Nuclear Engineering and Design, 350*, 182–194.

Oluwole, O. O., Gupta, A., Wu, B., Zhao, X., Meredith, K. V., & Wang, Y. (2021). Nongray models for radiative absorption and anisotropic scattering by water droplets in fire CFD simulations. *Fire Safety Journal, 120*, Article 103034.

OpenFOAM. (2018). User Guide v2112. https://www.openfoam.com/documentation/guides/latest/doc/guide-applications-solvers-heat-transfer-buoyantPimpleFoam.html. (Accessed 15 September 2022).

OpenFOAM v6 C++ source Guide. (2018). https://cpp.openfoam.org/v6/. (Accessed November 2022).

Patankar, S. V. (1980). *Numerical heat transfer and fluid flow*. Hemisphere Publishing Corporation.

Penndorf, R. (1957). Tables of the refractive index for standard air and the Rayleigh scattering coefficient for the spectral region between 0.2 and 20.0 μ and their application to atmospheric optics. *Journal of the Optical Society of America A: Optics and Image Science, 47*, 176–182.

Peters, B. (2002). Measurements and application of a discrete particle model (DPM) to simulate combustion of a packed bed of individual fuel particles. *Combustion and Flame, 131*, 132–146.

Peters, B., Baniasadi, M., Baniasadi, M., Besseron, X., Donoso, A. E., Mohseni, M., et al. (2019). XDEM multi-physics and multi-scale simulation technology: Review of DEM-CFD coupling, methodology and engineering applications. *Particuology, 44*, 176–193.

Pirker, D., Kahrimanović, S., & Goniva, C. (2011). Improving the applicability of discrete phase simulations by smoothening their exchange fields. *Applied Mathematical Modelling, 35*, 2479–2488.

Qi, F., & Wright, M. M. (2018). Particle scale modeling of heat transfer in granular flows in a double screw reactor. *Powder Technology, 335*, 18–34.

Radl, S., Gonzales, B. C., Goniva, C., & Pirker, S. (2014). State of the art in mapping schemes for dilute and dense Euler-Lagrange simulations. In *Proceedings of the 10th international conference on CFD in oil & gas* (pp. 103–112). Metallurgical and Process Industries.

Ren, C., Yang, X., Jia, H., Jiang, Y., & Xiong, W. (2017). Theoretical analysis of effective thermal conductivity for the Chinese HTR-PM heat transfer test facility. *Applied Sciences, 7*, 76.
Siegel, N., Gross, M., Ho, C., Phan, T., & Yuan, J. (2014). Physical properties of solid particle thermal energy storage media for concentrating solar power applications. *Energy Procedia, 49*, 1015–1023.
Stöcker, B., & Niessen, H. F. (1997). *Data sets of the SANA experiment 1994–1996, Tech. rep.* Forscungszentrum Jülich GmbH.
Sutherland, W. (1893). The viscosity of gases and molecular force. *Philosophic of Magnetic Series, 5*, 507–531.
Tausendschöen, J., & Radl, S. (2021). Deep neural network-based heat radiation modelling between particles and between walls and particles. *International Journal of Heat and Mass Transfer, 177*, Article 121557.
Tausendschöen, J., Stöckl, G., & Radl, S. (2023). Machine learning for heat radiation modeling of bi- and polydisperse particle systems including walls. *Particuology, 74*, 119–140.
Tavakkol, S., Zirwes, T., Denev, J. A., Jamshidi, F., Weber, N., Bockhorn, H., et al. (2021). An Eulerian-Lagrangian method for wet biomass carbonization in rotary kiln reactors. *Renewable and Sustainable Energy Reviews, 139*, Article 110582.
Tien, C. L., & Drolen, B. L. (1987). Thermal radiation in particulate media with dependent and independent scattering. *Annual Review Heat Transfer, 1*, 1–32.
Tolochko, N. K., Khlopkov, Y. V., Mozzharov, S. E., Ignatiev, M. B., Laoui, T., & Titov, V. I. (2000). Absorptance of powder materials suitable for laser sintering. *Rapid Prototyping Journal, 6*, 155–161.
ToolBox, E. (2004). Air - specific heat vs. Temperature at constant pressure. www.engineeringtoolbox.com/air-specific-heat-capacity-d_705.html. (Accessed 31 August 2022).
Viskanta, R., & Mengüç, M. P. (1987). Radiation heat transfer in combustion systems. *Progress in Energy and Combustion Science, 13*, 97–160.
Wang, S., & Shen, Y. (2022). Coarse-grained CFD-DEM modelling of dense gas-solid reacting flow. *International Journal of Heat and Mass Transfer, 184*, Article 122302.
Weller, H. G., Tabor, G., Jasak, H., & Fureby, C. (1998). A tensorial approach to computational continuum mechanics using object oriented techniques. *Computers in Physics, 12*, 620–631.
Yang, M., Zhang, J., Zhong, S., Li, T., Løvås, T., Fatehi, H., et al. (2022). CFD modeling of biomass combustion and gasification in fluidized bed reactors using a distribution kernel method. *Combustion and Flame, 236*, Article 111744.
Zhong, W., Yu, A., Zhou, G., Xie, J., & Zhang, H. (2016). CFD simulation of dense particulate reaction system: Approaches,recent advances and applications. *Chemical Engineering Science, 140*, 16–43.
Zhou, Z. Y., Kuang, S. B., Chu, K. W., & Yu, A. B. (2010). Discrete particle simulation of particle–fluid flow: Model formulations and their applicability. *Journal of Fluid Mechanics, 661*, 482–510.
Zhou, Z. Y., Yu, A. B., & Zulli, P. (2009). Particle scale study of heat transfer in packed and bubbling fluidized beds. *AIChE Journal, 55*, 868–884.